



Effect of confinement and interfacial adhesion on peeling of a flexible plate from an elastomeric layer



Bikramjit Mukherjee, Romesh C. Batra, David A. Dillard*

Department of Biomedical Engineering and Mechanics, M/C 0219, Virginia Polytechnic Institute and State University, Blacksburg, VA 24061, USA

ARTICLE INFO

Article history:

Received 24 March 2016

Revised 1 August 2016

Available online 6 September 2016

Keywords:

Elastomeric interlayer

Debonding

Cohesive zone model (CZM)

Instability

ABSTRACT

The finite element method and a cohesive zone model are used to analyze plane strain interfacial debonding of an elastomeric layer from an overhanging deformable plate when it is peeled off by applying a normal displacement at the edge of the overhang. The commercial software, ABAQUS, is employed in this work that is focused on understanding the collective role of the following two non-dimensional parameters: (i) the confinement parameter, α , defined in terms of the flexural rigidity of the plate, and the modulus and the thickness of the interlayer, and (ii) the adhesion parameter, ϕ , defined in terms of the cohesive zone parameters and the modulus to thickness ratio of the interlayer. The interfacial adhesion is characterized by a bilinear traction-separation (TS) relation. Numerical experiments reveal that when α is greater than α_c , damage initiates at an interior point on the interface and at the interface corner on the traction-free edge irrespective of the value of ϕ . However, ϕ must be greater than ϕ_c for the debonding to become wavy/undulatory. The critical value, ϕ_c , of the adhesion parameter agrees with the necessary condition found in our previous work on debonding of an elastomeric layer from a rigid block when it is uniformly pulled outward. For $\alpha < \alpha_c$, damage/debonding initiates only from the interface corner, and no wavy debonding ensues. The peak peeling force prior to the initiation of an internal debond is found to be a monotonically increasing function of ϕ/α , suggesting its potential use as a design variable and as a guide for determining the TS parameters. Results of a few additional numerical experiments in which the elastomeric layer can debond from both adherends provide insights into designing a demolding process for a sandwiched elastomeric layer.

© 2016 Elsevier Ltd. All rights reserved.

1. Introduction

A soft elastomeric interlayer sandwiched between two adherends is encountered in a wide variety of engineering applications such as manufacturing of bio-implants, micro-printing processes, and modern bio-inspired adhesive systems. The requirement of controlling interfacial separation of the confined interlayer in such applications necessitates understanding collective roles of the geometric, the material, and the interfacial adhesion parameters on the initiation and propagation of interfacial debonding of the interlayer from the adherend(s).

It is well known that the lateral constraint imposed by the geometric confinement plays a crucial role in the adhesion/debonding characteristics of a sandwiched interlayer. An often studied problem in this context is the debonding of a rigid cylindrical adherend from a deformable interlayer attached to a fixed base, shown schematically in Fig. 1a. It has been shown (Messner, 1963;

Crosby et al., 2000) that the ratio, a/h , of the adherend radius (a) to the interlayer thickness (h) and the compressibility (Lai et al., 1992; Gent, 1994) of the interlayer material quantify confinement and determine the traction distribution at the interface. For small values of a/h ($< \sim 1$), the singularity at the corner (edge) on the traction-free edge dominates the distribution of the normal traction (peel stress) at the interface. Therefore, for axisymmetric deformations a crack initiates at the edge and propagates towards the center. However, for larger values of a/h ($> \sim 1$) and a near-incompressible interlayer, the peel stress has a peak value at the center with a small singularity-dominant region at the edge, and the debonding initiates from an interior point. Experimental investigations by Webber et al. (2003) and Anderson et al. (1974) support these statements.

Peeling of a flexible plate from an elastomeric interlayer (Fig. 1b) is another problem of practical interest in which the confinement has been shown to play a major role in the debonding process (Lefebvre et al., 1988; Adda-Bedia and Mahadevan, 2006; Chatak, 2006). Even when stresses in the external edge region become high because of the peeling action, the interlayer confinement and the internal debonding control the failure process.

* Corresponding author. Fax: +1 540 231 9187.

E-mail address: dillard@vt.edu (D.A. Dillard).

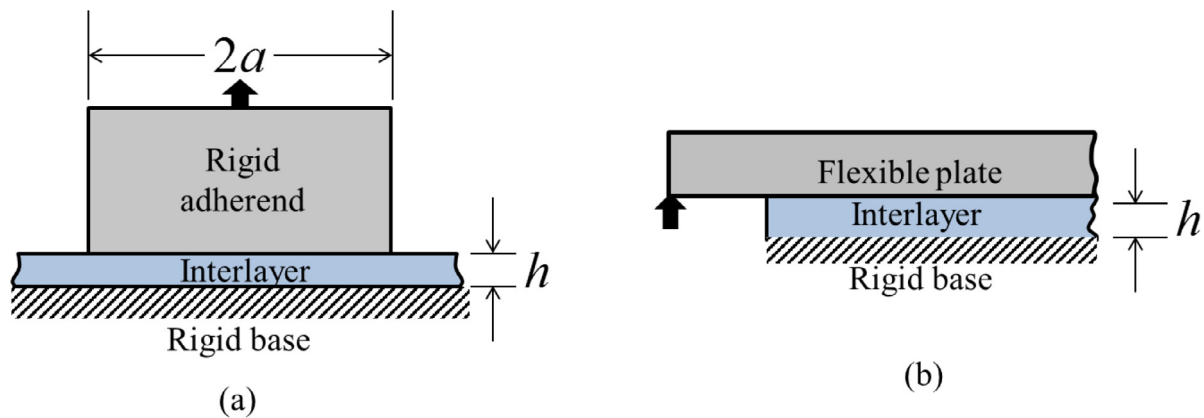


Fig. 1. Schematic sketches of (a) a probe-tack configuration, and (b) a flexible plate peeled from a thin elastomeric layer bonded to a fixed rigid base (Colored figures in the web version only).

It has been suggested that the ratio of the lengths, $(D_p/\mu)^{1/3}$ and h describes the geometric confinement. Here D_p is the flexural rigidity of the deformable plate, and μ the shear modulus of the interlayer. A large confinement is found to be relieved by the nucleation of debonding at a location away from the edge (Ghatak and Chaudhury, 2003).

While the geometric confinement significantly affects the adhesive debonding mechanisms of a sandwiched layer, its intricate coupling with the interfacial adhesion must be understood to delineate the debonding process. For example, in the debonding phase of a probe tack test (Fig. 1a), the geometric confinement, a/h , and the dimensionless descriptor of adhesion, $\mathcal{G}_c/\mu a$, where \mathcal{G}_c is the critical strain energy release rate of the interface, collectively govern the debonding behavior. For a large value of $\mathcal{G}_c/\mu a$ dictated by the degree of confinement (Creton and Lakrout, 2000; Crosby et al., 2000; Creton et al., 2001) cavities have been observed to initiate within the bulk interlayer. For highly confined films and relatively weak interfaces, the internal adhesive debonding often involved nucleation of multiple cavities at the interface and their eventual coalescence into a crack (Creton and Lakrout, 2000; Yamaguchi et al., 2007). Even though these internal debonds were initially thought to have initiated from local defects. The analyses of Ghatak et al. (2000), Mönch and Herminghaus (2001), and Shenoy and Sharma (2001) suggested that they are adhesion-induced instabilities that occur when the interfacial effects dominate over elastic deformations of the interlayer. This determines spacing between the cavities that scales with the thickness of the interlayer. An approximate analysis showed that the coalescence behavior of the adjacent cavities is governed by $\mathcal{G}_c/\mu a$ and its large value impedes lateral propagation of the interfacial cracks and results in fibrillation (Creton et al., 2001). When a flexible plate is peeled from an elastomeric layer (Fig. 1b), the adhesion-induced instability initiating and growing over the stressed zone results in fingerlike debonding (Ghatak and Chaudhury, 2003; Vilmin et al., 2009). The spacing between two adjacent fingers scales with the interlayer thickness and their length in the peeling direction with $(D_p/\mu)^{1/3}$. Adda-Bedia and Mahadevan (2006) and Ghatak (2006) have proposed that the spacing between two adjacent fingers does not depend on the interfacial adhesion. However, the coupling between the geometric confinement and the adhesion on debonding for this problem has not been thoroughly studied. Here we attempt to address this coupling by numerical simulations of the peeling problem.

A frequently used technique for studying debonding employs a cohesive zone model (CZM) (Dugdale, 1960; Barenblatt, 1962; Ungsuwarungsri and Knauss, 1987; Xu and Needleman, 1995). In a CZM the interaction of adjoining points at an interface is phe-

nomenologically represented by a spring of zero-length that softens after it has been extended by a prescribed value (reached a peak traction) and breaks at a pre-specified value of the extension (when the fracture energy criterion is met). It involves prescribing *a-priori* a relation between the surface traction and the corresponding separation/displacement-jump (relative displacement of two adjoining points) at the interface. For a given mode of debonding, two parameters, namely the fracture energy (\mathcal{G}_c) and the peak traction (T_c) characterize commonly used traction-separation (TS) relations (Dugdale, 1960; Ungsuwarungsri and Knauss, 1987; Xu and Needleman, 1995; Geubelle and Baylor, 1998). With a CZM both the nucleation of debonding and its propagation can be simulated. The CZM bridges the gap between the classical linear elastic fracture mechanics (LEFM) and the stress-based approach (Anderson, 2005) of predicting failure. Whereas \mathcal{G}_c can be deduced from the test data (Kaelble, 1965; Ghatak et al., 2005), it is not easy to estimate values of other parameters in the TS relation for a given interface. An iterative (brute-force) approach (Li et al., 2005; Turon et al., 2007; Tsai et al., 2014) is often used to find the TS relation which, when used in numerical simulations, predicts well the experimental load-displacement curve. Digital image correlation (Shen and Paulino, 2011), interferometry (Gowrishankar et al., 2012), and molecular dynamics simulations (Zhou et al., 2008; Sinko and Keten, 2015) have been used to extract values of parameters in the TS relation.

Here we use the finite element method (FEM), the CZM and a bilinear TS relation, to study debonding of a flexible plate from an elastomeric layer that is assumed not to debond from a rigid base, e.g., see the configuration shown in Fig. 1b. The commercial FE software, ABAQUS, and the CZM already imbedded in it is used to analyze the problem. Mukherjee et al. (2016a) have recently analyzed with the CZM and a bilinear TS relation wavy debonding during plane strain deformations of an infinitely wide confined elastomeric layer from a rigid adherend pulled upwards using a configuration similar to that shown in Fig. 1a. They found that the large peeling traction over the central region induced a damage (cohesive) zone over which wavy/undulatory debonding ensues due to competition between the interfacial softening and the elastic deformations of the interlayer. A necessary condition for homogeneous deformations of the incompressible interlayer to become unstable (undulatory debonding/adhesion-induced instability) is that the parameter $\phi = T_c^2 h / E \mathcal{G}_c$ exceed approximately 4.15, where $E = 3\mu$ is Young's modulus of the interlayer material. This condition implies that for a given adhesion and interlayer material, its thickness must exceed a critical value for an interfacial instability to occur.

During peeling of an overhanging flexible plate from an elastomeric layer with the displacement applied at the edge of the overhang, the bending of the plate results in a stressed zone of characteristic length $(D_p/\mu)^{1/3}$ near the traction free edge of the interlayer. Results of Ghatak and Chaudhury (2003) and Adda-Bedia and Mahadevan (2006) for peeling of a flexible plate suggest that the interlayer thickness must be smaller than a critical value dictated by the length $(D_p/\mu)^{1/3}$ for an undulatory debonding to ensue. This and the aforementioned necessary condition, $h > 4.15EG_c/T_c^2$, determine whether or not debonding will be undulatory. This reiterates the importance of coupling between confinement and adhesion when studying debonding in this problem. The analysis of the peeling of an overhanging plate from an elastomeric layer by using a TS relation for the interface enables us to probe this coupling.

The text in this paragraph was suggested by an anonymous reviewer. We note that the problem of peeling of a plate from an elastomeric layer constrained to a rigid base (Fig. 1b) is inherently mixed-mode. In the absence of an interlayer (which defines the global mode-mixity), this configuration involves a phase angle of -36° (Li et al., 2004). Considering an infinitely thin interlayer makes the phase angle even more negative (Suo and Hutchinson, 1989), with the extent depending on the Dundurs parameter between the plate and the interlayer. Thicker interlayers can generally be expected to return the mode-mixity towards the global value but not beyond it. In our analysis of interfacial damage/debonding, we will assume that the interface fails dominantly in tension (peel stress).

Results of numerical experiments for studying the collective effect of confinement and adhesion reported here advance our current understanding of the peeling phenomenon, help in developing predictive models for complex manufacturing processes involving separation of confined elastomeric layers, shed light on the global behavior such as the pull-off force as a function of the geometric confinement and interfacial adhesion and its transition from a strength-dominated regime to a fracture-energy dominated regime, and may help in determining the TS parameters for the interface between an elastomeric layer and a stiff adherend.

The rest of the paper is organized as follows. We describe in Section 2 the problem studied, outline in Section 3 the numerical approach used to solve the problem, and present and discuss in Section 4 results obtained by the FEM that relate the damage growth and debonding to the confinement and the interfacial adhesion. The findings are summarized in Section 5. The Appendices include mesh refinement studies, energy balance for one example problem, results of some three-dimensional (3-D) problems that support conclusions drawn from the analysis of 2-D problems, computed peel stress distribution for an example problem in which the shear interaction is considered, and the sensitivity of results to slight compressibility of the elastomeric layer.

2. Formulation of the problem

A schematic sketch of the problem studied is shown in Fig. 2. The domain of interest consists of an elastomeric layer sandwiched between a deformable plate and a fixed rigid base. It is assumed that debonding occurs only at the interface between the plate and the interlayer. Neglecting body and inertia forces¹, equations of motion in the rectangular Cartesian coordinate axes $(x, y, z$ or $x_1,$

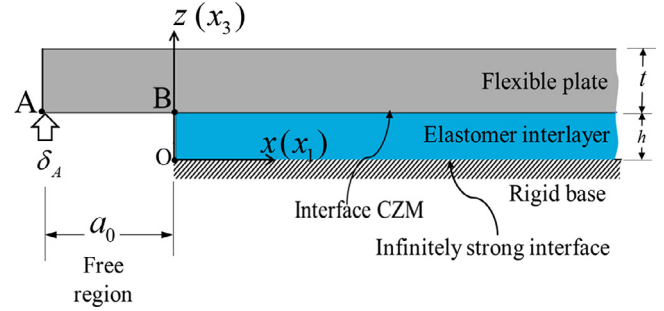


Fig. 2. Schematic sketch of the problem studied.

x_2, x_3 shown in Fig. 2) are

$$\frac{\partial \sigma_{ij}}{\partial x_j} = 0, \quad i = 1, 3, \tag{1}$$

where σ_{ij} is the stress tensor and a repeated index implies summation over the range of values of the index. The plate and the interlayer materials are assumed to be homogeneous, isotropic and Hookean², and the elastomeric layer is also assumed to be incompressible. Constitutive equations are

$$\text{Flexible plate: } \sigma_{ij} = \frac{2\mu_p \nu_p}{(1 - 2\nu_p)} \varepsilon_{kk} \delta_{ij} + 2\mu_p \varepsilon_{ij}, \tag{2}$$

$$\text{Interlayer: } \sigma_{ij} = -p\delta_{ij} + 2\mu \varepsilon_{ij} \tag{3}$$

Here μ_p and ν_p are, respectively, the shear modulus and Poisson's ratio of the flexible plate, μ the shear modulus of the elastomeric interlayer, p the hydrostatic pressure in the elastomeric layer arising due to the incompressibility constraint, δ_{ij} the Kronecker delta, and ε_{ij} the strain tensor for infinitesimal deformations defined as $\varepsilon_{ij} = \frac{1}{2} (\frac{\partial u_i}{\partial x_j} + \frac{\partial u_j}{\partial x_i})$, where u_i is the displacement along the x_i -axis.

The system is assumed to be very wide in the y -direction so that a plane strain state of deformation prevails³ in the xz - (or x_1x_3 -) plane, i.e., $u_y = 0$ and the deformation is uniform along the y -direction. All displacement components at points on the lower surface, $z = 0$, of the interlayer are assumed to be zero to simulate no debonding at its interface with the stationary rigid base. A monotonically increasing vertical peeling displacement⁴, δ_A , is applied at the tip point, A, of the flexible plate. These displacement boundary conditions are written as

$$\text{Lower surface } (z = 0) \text{ of the interlayer: } u_x = u_z = 0 \tag{4}$$

$$\text{Point A: } u_z = \delta_A \tag{5}$$

The remaining bounding regions that include the overhang AB (of length a_0) of the plate and the right edge of the system are assumed to be traction-free, i.e.,

$$T_i = \sigma_{ij} n_j = 0 \tag{6}$$

where n_j denotes the j^{th} component of the unit outward normal at a point on the bounding surface.

² The maximum computed strain, except possibly at points near the edges where singularities may occur, in our simulations is 6%. Thus it is reasonable to assume the interlayer material to be linear elastic.

³ As will be shown later, a plane strain deformation cannot accurately predict details of debonding after an interfacial instability has set in. A three-dimensional analysis is needed for finding these details.

⁴ In linear elasticity one should apply displacements on a surface of finite area. Thus our applying vertical displacement δ_A at points on the edge of the lower surface of the flexible plate is an approximation. In the numerical solution of the problem, one can easily satisfy this boundary condition.

¹ Since the time of interest is much larger than the time taken for an elastic wave to traverse the elastomeric layer thickness several times, inertia terms are neglected in the equations of motion.

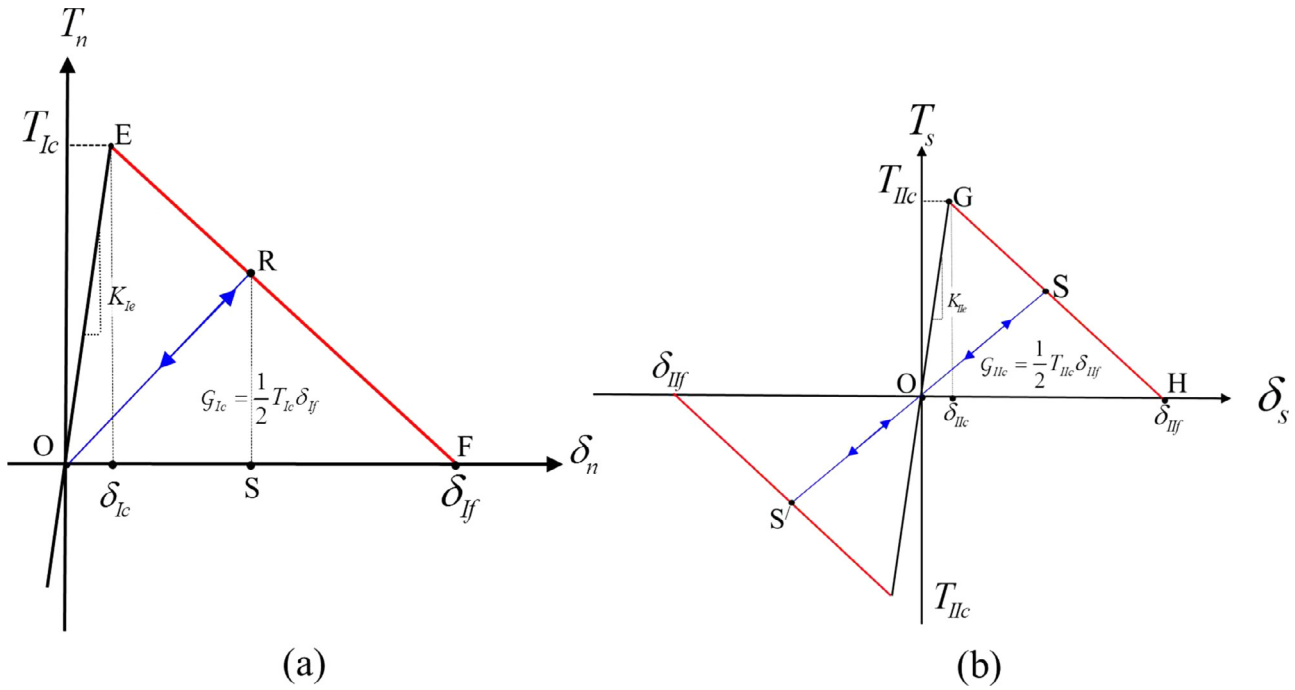


Fig. 3. For pure mode-I and mode-II deformations, bilinear traction-separation relations (a) between the interfacial normal traction and the jump (contact-opening) in the interface normal displacement and (b) between the interfacial tangential traction and the displacement jump in the tangential direction (sliding).

The interaction at the interface between the plate and the interlayer is modelled by a TS relation that relates the interfacial traction components to the displacement jump components. Bilinear TS relations (Geubelle and Baylor, 1998) for pure modes I and II shown in Fig. 3 are given by

$$T_n(\delta_n) = \begin{cases} K_{ie}\delta_n & (\delta_n \leq \delta_{ic}) \\ \frac{T_{ic}}{\delta_{if} - \delta_{ic}}(\delta_{if} - \delta_n) & (\delta_{ic} \leq \delta_n \leq \delta_{if}) \\ 0 & (\delta_{if} \leq \delta_n) \end{cases}$$

$$T_s(\delta_s) = \begin{cases} K_{Iie}\delta_s & (-\delta_{IIc} \leq \delta_s \leq \delta_{IIc}) \\ \frac{T_{IIc}}{\delta_{IIf} - \delta_{IIc}}(\delta_{IIf} - \delta_s) & (\delta_{IIc} \leq \delta_s \leq \delta_{IIf}) \\ \frac{T_{IIc}}{\delta_{IIf} - \delta_{IIc}}(-\delta_{IIf} - \delta_s) & (-\delta_{IIf} \leq \delta_s \leq -\delta_{IIc}) \\ 0 & (\delta_{IIf} \leq \delta_s, \delta_s \leq -\delta_{IIc}) \end{cases} \quad (7)$$

Fig. 3a and b depict, respectively, the TS relations for the pure opening mode (mode-I) and the pure sliding mode (mode-II). The normal traction, T_n , (tangential traction, T_s) increases linearly with the interfacial normal (sliding) displacement jump/opening, δ_n , (δ_s), along the line OE (OG). The slope is denoted as K_{ie} (K_{Iie}).

During mixed-mode deformations, damage/softening initiates at an interfacial point when

$$\frac{\langle T_n \rangle^2}{T_{ic}^2} + \frac{T_s^2}{T_{IIc}^2} = 1, \quad (8)$$

where the Macaulay bracket, $\langle \cdot \rangle$, signifies that the normal traction, when tensile, contributes to damage initiation, and T_{ic} (T_{IIc}) is the prescribed peak value of T_n (T_s). After reaching its peak value T_{ic} (T_{IIc}), the normal (tangential) traction decreases affinely with an increase in the normal (sliding) displacement until the plate separates from (slides on) the interlayer at δ_{if} (δ_{IIf}).

The debonding initiates at an interfacial point when

$$\frac{G_I}{G_{ic}} + \frac{G_{II}}{G_{IIc}} = 1, \quad (9)$$

where $G_I = \int_0^{\delta_n} T_n d\delta_n$ and $G_{II} = \int_0^{\delta_s} T_s d\delta_s$ are the energy release rates (ERRs) for modes I and II, respectively, and $G_{ic} = \frac{1}{2} T_{ic} \delta_{if}$ and $G_{IIc} = \frac{1}{2} T_{IIc} \delta_{IIf}$ are the corresponding critical ERRs equal to areas of triangles OEF and OGH, respectively. Should unloading occur for normal (sliding) displacement values between those for points E and F (G and H), the normal (tangential) traction decreases following the path RO (SOS'). Subsequent reloading causes the traction to follow the path OR (S'/OS).

The total energy of separation at the initiation of debonding at a point is given by $\mathcal{G} = G_I + G_{II}$. In terms of phase-angle of mode-mixity, defined as $\varphi = \tan^{-1}(\sqrt{G_{II}/G_I})$, and using Eq. (9), one can write $\mathcal{G}/G_{ic} = (1 + \tan^2 \varphi)/(1 + \tan^2 \varphi(G_{ic}/G_{IIc}))$. A complete description of the CZM and the TS relations for mixed-mode loading including paths followed during unloading and reloading is given in Camanho et al. (2003). Xiao and Batra (2014) adopted Camanho et al.'s approach to study delamination in a sandwich structure subjected to water slamming loads.

Following Maugis (1992) and Tang and Hui (2005), we assume that the interface fails in tension; thus we set $T_{ic} \ll T_{IIc}$ and $G_{ic} \ll G_{IIc}$. Under this assumption, damage initiates when the peel stress exceeds T_{ic} and debonding occurs when $G_I = G_{ic}$. Henceforth, we use symbols δ_f , δ_c , G_c , and T_c for δ_{if} , δ_{ic} , G_{ic} , and T_{ic} , respectively. Results computed for one case with $T_{ic} = T_{IIc}$ and $G_{ic} = G_{IIc}$ are included in Appendix D.

In general, values of the initial slopes K_{ie} and K_{Iie} must be sufficiently large (Song et al., 2006) to minimize the artificial compliance introduced into the system and to avoid inter-penetration under compression. Very large values of K_{ie} and K_{Iie} can make the system matrices ill-conditioned when the problem is analyzed by the FEM. We set $K_{ie} = K_{Iie} = K_e$ in the remainder of the paper.

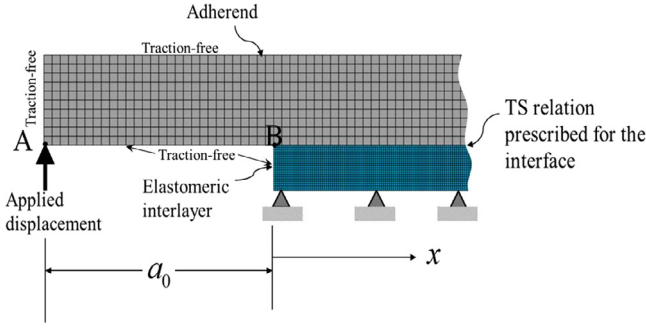


Fig. 4. The FE mesh and the boundary conditions on the region whose plane-strain deformations are analyzed.

At an interfacial point where the displacement jump exceeds δ_c , the ratio of the ERR to the total fracture energy, $D = 1 - \frac{(\delta_f - \delta)^2}{\delta_f(\delta_f - \delta_c)}$ = (area of portion OERS)/(area of triangle OEF), is termed as the ‘extent of damage’ when discussing results.

Eqs. (1)–(9) define the boundary value problem (BVP) analyzed in this work. The possibility of debonding at *a priori* unknown points on the interface makes the BVP challenging.

3. Numerical solution of the problem

3.1. Approach

The commercial FE software ABAQUS/Standard (version 6.11–2)⁵ (Hibbitt and Sorensen, 2012) is used to numerically analyze the BVP by employing 4-node square/rectangular elements in the FE mesh shown in Fig. 4. In the ABAQUS terminology we use CPE4 (plane strain, 4-point integration) elements for the plate and the CPE4H (H stands for hybrid formulation appropriate for incompressible materials in which both displacements and the pressure are taken as unknowns) elements for the interlayer. Sensitivities of the computed peel stress distributions and the load-displacement variations to the FE mesh are reported in Appendix A. The vertical displacement δ_A of point A in Figs. 2 and 4, is gradually increased. A surface-based cohesive contact interaction (Hibbitt and Sorensen, 2012) is used for the interface between the flexible plate and the interlayer⁶. We have not captured a converged value of the order of singularity (Bogy, 1968; Dundurs, 1969; Chadegani and Batra, 2011) at the initial debond tip ($x = 0$). However, key findings reported herein are found to be insensitive to further refining the FE mesh (see Appendix A). In order to alleviate numerical instabilities and associated convergence difficulties, the “Damage Stabilization” option (viscous regularization) in ABAQUS is used. Unless otherwise mentioned, the value of the stabilization parameter was chosen to be 10^{-7} ; using a lower value was found not to affect the computed results but significantly increased the computation time.

4. Results and discussion

4.1. Choice of parameters

When a_0 is held constant and bending is assumed as the dominant mode of deformation of the plate, there are the following four

⁵ The computed results satisfied energy balance with ~8% discrepancy between the external work and the sum of the strain energy, the dissipation due to interfacial damage, and the dissipation due to viscous regularization (Appendix B).

⁶ In ABAQUS terminology it means that the plate surface is defined as the ‘master’ surface and the interlayer surface as the ‘slave’ surface. While computing the displacement jump at a slave node, the displacement of the closest point on the master surface is computed by interpolating the displacements of neighboring nodes.

independent length scales⁷:

$$h, (D_p/\mu)^{1/3}, \delta_f, G_c\mu/T_c^2$$

The flexural rigidity of the plate, D_p , is given by $D_p = E_p t^3/12(1 - \nu_p^2)$ where E_p is Young’s modulus of the plate material, ν_p Poisson’s ratio and t the plate thickness (ν_p and t are held constant in our analysis). The geometric mean, $\sqrt{h(D_p/\mu)^{1/3}}$, of the listed first two lengths quantifies the characteristic stress decay distance (Dillard, 1989; Ghatak et al., 2005) from the edge, and their ratio, $\alpha = (D_p/\mu h^3)^{1/3}$, signifies confinement (Ghatak, 2006) of the interlayer. The ratio of h and the CZM length scale $G_c\mu/T_c^2$ yields the parameter $\phi = T_c^2 h/G_c E$ (note that $E = 3\mu$ for the incompressible elastomeric layer) that determines the necessary condition for the onset of contact instability (Mukherjee et al., 2016a) during plane strain deformations of the elastomeric layer sandwiched between two rigid blocks and one rigid block pulled away from it and the other kept stationary. Following Adda-Bedia and Mahadevan (2006), Ghatak (2006), Vilmin et al. (2009), we call α the confinement parameter and following Mukherjee et al. (2016a) ϕ the CZM/adhesion parameter.

Besides α and ϕ , the nondimensional parameters defined below are used in the presentation of results.

$$\bar{T}_i = \frac{T_i}{T_c}, \Delta_A = \frac{\delta_A}{\delta_f}, \bar{P}_A = \frac{P_A}{D_p \beta^3 \delta_f}, X = x\beta, A_0 = a_0\beta$$

where T_i stands for either the normal (T_n) or the tangential traction (T_s) at the interface, P_A is the reaction force at point A and $\beta = (12\mu/D_p h^3)^{1/6}$.

Our objective is to explore effects of α and ϕ on the debonding process. We achieve this by setting, unless otherwise specified, $\beta^{-1} = 1$ mm, $\mu = 5$ MPa, $\nu_p = 0.3$, $t = 1$ mm, $a_0 = 2.83$ mm, the plate length = 50 mm, $T_c = 1.265$ MPa and $K_e = 10^6$ N/mm³. For desired values of α and ϕ , we set $h = 12^{1/6} \beta^{-1} \alpha^{1/2}$, $D_p = 12^{1/2} \mu \beta^{-3} \alpha^{3/2}$, and $G_c = T_c^2 h/3\phi\mu$.

4.2. Analysis of interfacial tractions with no damage allowed at the interface

In this sub-section, we report interfacial tractions as a function of the confinement when the flexible plate is peeled away from the interlayer but no separation is allowed to occur at the interface. Results are computed for constant vertical displacement, $\delta_A = 1\mu\text{m}$, at different values of the confinement parameter, α ⁸. A very large value is assigned to T_c so that damage does not initiate for $\delta_A = 1\mu\text{m}$ and the FE mesh used⁹.

The distributions (nodal values) of T_n (peel stress) and T_s (tangential/shear stress) are plotted in Fig. 5 as a function of the distance x from the corner point B. With an increase in α , the peel stress, in addition to the large value exhibited at corner B, has a local maximum (secondary/internal peak) where the tangential stress is nearly zero. One can note that the hydrostatic pressure, p , plotted for $\alpha = 8$, significantly contributes to the normal stresses

⁷ In order to understand the length scale of (cf. Fig. 4) singularity oscillations (near corner B) in the interfacial tractions, we recall that the solution is of the form $\sin(\frac{1}{2\pi} \ln \frac{1-\beta_D}{1+\beta_D} \ln r)$ where r is the radial distance from point B, and $\beta_D = \frac{1}{2} \frac{\mu_p(1-2\nu)-\mu(1-2\nu_p)}{\mu_p(1-\nu)+\mu(1-\nu_p)}$ is Dundurs parameter, where μ_p is the shear modulus of the flexible plate and ν Poisson’s ratio of the interlayer. For materials of interest here, $\nu \approx 0.5$, $\nu_p \approx 0.3 - 0.4$, $\mu/\mu_p \approx 10^{-5}$, we get $\beta_D \approx 0$.

⁸ The FE height was adjusted as the interlayer thickness was modified to vary confinement, however, at least 10 elements were placed through the interlayer thickness. Rectangular elements had aspect ratio less than 4.

⁹ One example is $\mu = 5$ MPa, $h=0.67$ mm, $t = 1$ mm, $E_p = 2.115$ GPa, $\nu_p = 0.3$, $T_c = 10$ MPa and $K_e = 10^6$ N/mm³. For these values of parameters, the damage does not initiate when elements of dimensions 0.0125 mm \times 0.0125 mm and 0.1 mm \times 0.1 mm are used to discretize the interlayer and the flexible plate, respectively.

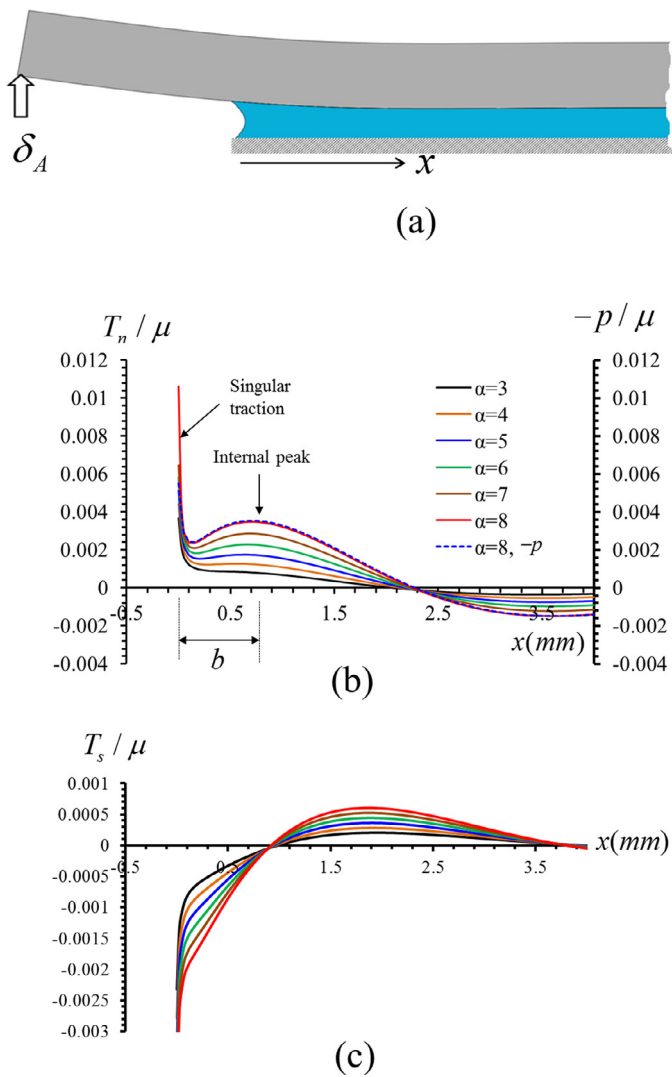


Fig. 5. (a) A schematic sketch of the deformed shape of the specimen; the computed (b) interfacial normal traction (T_n) and (c) the interfacial tangential traction (T_s) as functions of the distance x from the corner point B for different levels of confinement, α . These results correspond to a very high value of the interfacial strength to prevent debonding at the interface.

including the peel stress and accounts for the large difference between the normal and the tangential stresses. For low confinement (e.g., $\alpha = 3$), the local maximum of peel stress is not exhibited, though evidence of a shoulder remains.

The computed distribution of the interfacial peel stress is compared in Fig. 6 with that from approximate ‘mechanics of materials’ (MoM) solutions of other investigators. The approximate solution of Ghatak et al. (2005) captures qualitatively the interfacial normal traction distribution for low values of α . The solution of Ghatak et al. (2004), who enforced a boundary condition of zero peel stress at point B, captures the location of the secondary peak for confined interlayers. In a subsequent work Ghatak et al. (2005) assumed that the peel stress had a local maximum at point B. As shown by Adda-Bedia and Mahadevan (2006), a MoM solution fails to capture details of interfacial tractions near the edge.

The non-dimensional distance, $b\beta$, from point B where the local maximum in T_n occurs for sufficiently confined interlayers, is computed for a range of values of α and β , and plotted in Fig. 7 as a function of α . It can be seen that $b\beta$ becomes relatively insensitive to the confinement level for large values of α . For the experimental set-up of Ghatak et al. (2004), $\alpha > 15$, our prediction

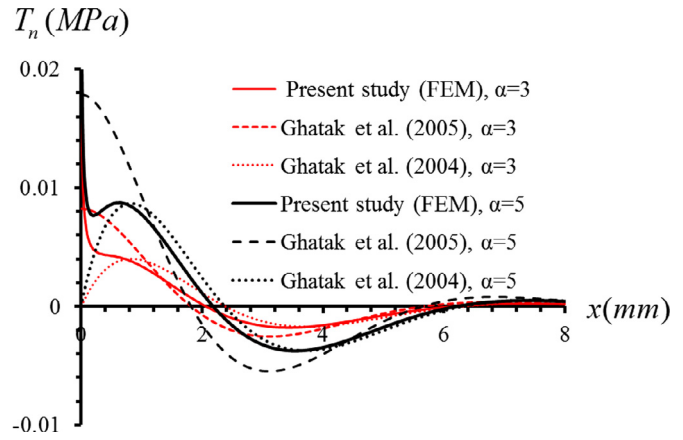


Fig. 6. Comparison of the present results with those from the literature for $\alpha = 3$ and 5. These results correspond to a very high value of the interfacial strength to prevent debonding at the interface.

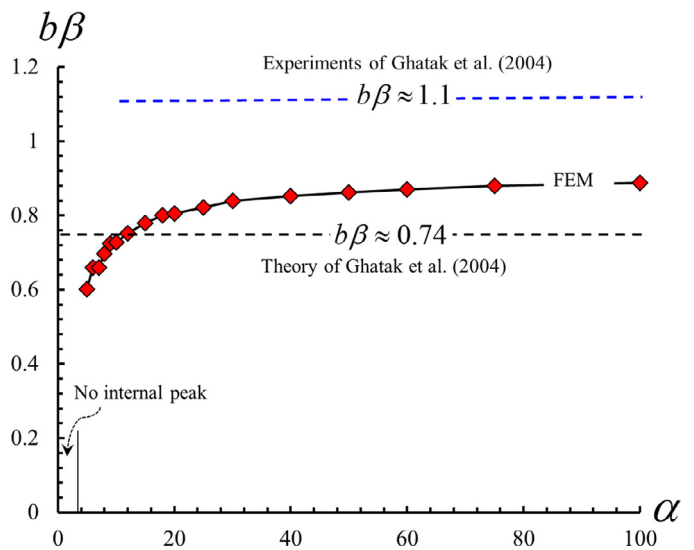


Fig. 7. Non-dimensional location of the internal peak as a function of the confinement level. These results correspond to very high value of the interfacial strength to prevent debonding at the interface.

of this distance lies between the experimentally measured, $b\beta \approx 1.1$, and the approximate theoretical prediction, $b\beta \approx 0.74$ (Ghatak et al., 2004). The assumption $b\beta \approx \text{constant}$ leads to the relation, $b \propto (E_p/E)^{1/6}(t)^{1/2}(h)^{1/2}$, which is similar to the characteristic lag distance $l_{\text{shear-lag}} \propto (E_p/E)^{1/2}(t)^{1/2}(h)^{1/2}$ found from Volkersen’s shear lag analysis (Anderson et al., 1977). This correlation is understandable in that the internal peak in the peel stress occurs because shear stresses at the interface transfer load into the elastomer interlayer through shear lag but in a decreasing traction field; e.g., see the analysis of a beam on an elastic foundation (6th order differential equation (Dillard, 1989)).

As pointed out by an anonymous reviewer of an earlier version of this paper, a slight departure from incompressibility of the interlayer may significantly affect distributions of the interfacial tractions (Lai et al., 1992; Tizard et al., 2012). Results of some numerical experiments addressing this are included in Appendix E.

4.3. Analysis of damage growth and debonding

In the CZM, damage initiates at an interfacial point when the peel stress there just exceeds the prescribed peak traction, T_c . A further increase in the applied displacement δ_A causes the peel

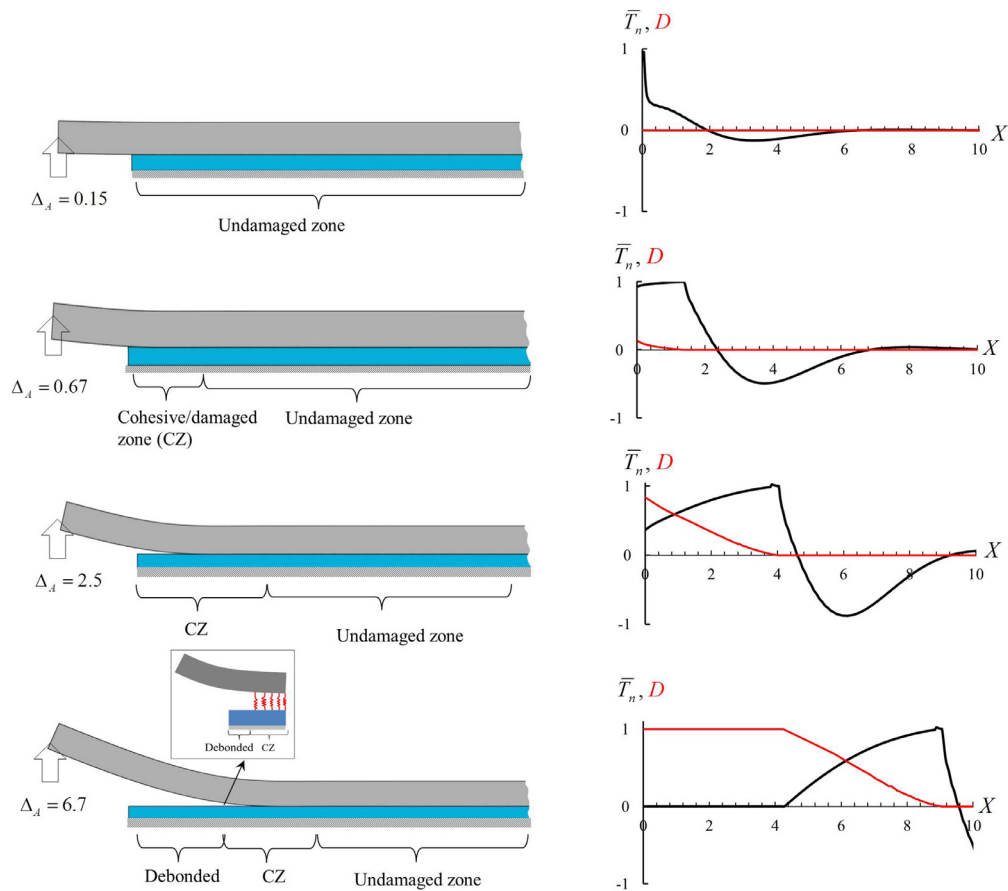


Fig. 8. For $\alpha = 3$, $\phi = 0.1$, distributions of the non-dimensional normal traction ($\bar{T}_n = T_n/T_c$) and the extent of damage (D) at the interface as a function of the non-dimensional distance (X) measured from point B at increasing values of the non-dimensional applied displacement (Δ_A). The deformed configurations, shown on the left, have been exaggerated by a factor of 5. This is an example of type-1 debonding mechanism shown in Fig. 13. Note that the CZ ($\delta_c < \delta_n < \delta_f$, $0 < D < 1$) is a partially damaged region and is not traction-free. Two adjoining surfaces of the CZ can be thought of as being held by stretched springs, as shown in the inset.

stress at that point to follow the softening segment EF of the TS relation in Fig. 3. The region where softening (sometimes called damage) has occurred in the TS relation is henceforth referred to as the cohesive zone (CZ). It is conjectured that for large values of α the damage/softening initiation at the corner point B is accompanied by the initiation of damage at an interior point situated at a distance b (analogous to the shear-lag distance) from point B due to the local peak peel stress there increasing with α . The literature results (Bao and Suo, 1992; Hill et al., 2003; Mukherjee et al., 2016a) suggest that the post-damage response will be influenced by the value of parameter ϕ . In order to delineate the collective role of α and ϕ on the damage/debonding behavior, we simulate progressive debonding with a gradual increase of δ_A .

4.3.1. Damage and debonding mechanisms

Fig. 8 exhibits the evolution of the peel stress and the extent of damage with a monotonic increase in the applied displacement δ_A when $\alpha = 3$ and $\phi = 0.1$ ¹⁰. With increasing δ_A applied at the plate edge¹¹, damage initiates at the corner B and forms a CZ accompanied by a redistribution of the stress. Note that the peel stress at

point B is now limited by the peak traction T_c in the TS bilinear relation. With continued loading the contact opening at point B reaches the ultimate value δ_f , the peel stress vanishes and the plate is debonded there from the elastomer. The further increase in δ_A results in the propagation of this debond with a CZ at its front. This edge debonding, named type-1 for later reference, has been studied by a semi-analytical method using a CZM by Mukherjee et al. (2016c) who extended techniques of Dillard (1989) and Ghatak et al. (2005). Their results reveal that the CZ size increases with an increase in the quantity α/ϕ . For small values of α/ϕ , the CZ size becomes vanishingly small and the edge debonding process can be analyzed by the LEFM approach, e.g., see Ghatak et al. (2005).

In Figs. 9–11 we have plotted for $\phi = 4, 5$, and 50 , respectively, computed evolutions of the interfacial peel stress and the extent of damage, D , for a very high level of confinement, $\alpha = 100$. Results shown in Fig. 9 reveal that the damage initiation and the concomitant CZ formation over a negligibly small region at the edge are accompanied by the damage initiating internally at a distance 0.85 (consistent with the results shown in Fig. 7) from point B and spreading of a CZ due to the local peak peel stress there. As δ_A is increased further, the internal CZ coalesces with the edge CZ, and the resulting debond propagates with one CZ at its front. This qualitatively agrees with the experimental finding that debonds initiate internally and eventually coalesce with

¹⁰ It has been checked that the computed results are stable with respect to variations in the TS parameters. For example, $\alpha = 100$, $\phi = 4$, $\beta^{-1} = 1$ mm, $\mu = 5$ MPa, $K_e = 10^6$ N/mm³, $T_c = 1.265$ MPa, and $\Delta_A = 0.7$, the maximum % changes in nodal values of the peel stress over the internal CZ were found to be 0.02% and 4.58% when $T_c = 1.266265$ MPa and $K_e = 10^8$ N/mm³ were used, respectively.

¹¹ An infinitesimal displacement should cause a CZ to initiate at point B since linear elasticity theory implies a singular traction at point B. However, in an FE simulation using a CZM, the value of the applied displacement required to initiate a CZ

at point B depends upon the FE mesh used because the singular peel stress cannot exceed T_c .

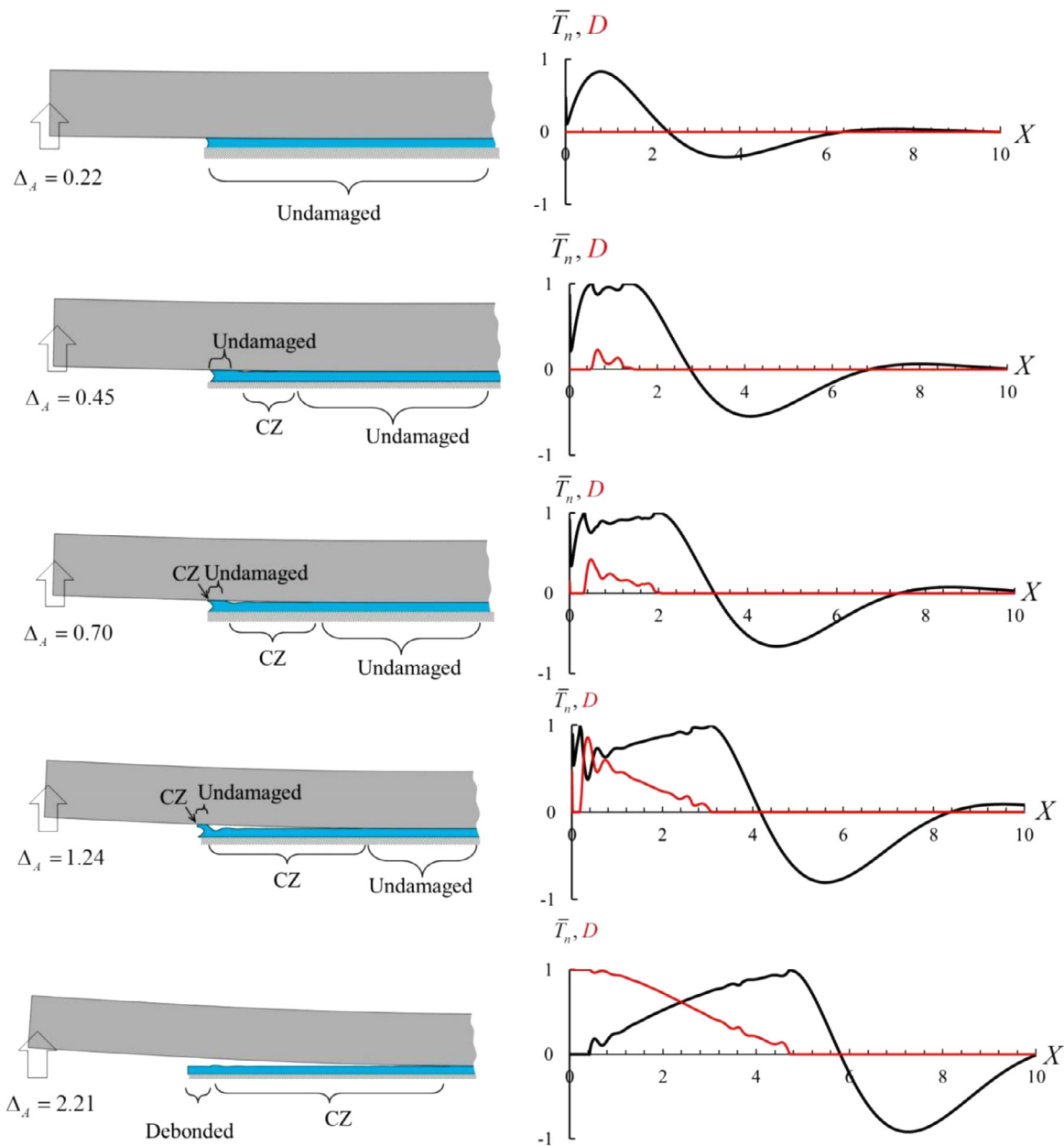


Fig. 9. For $\alpha = 100$, $\phi = 4$, distributions of the non-dimensional normal traction (\bar{T}_n) and the extent of damage (D) at the interface as a function of the non-dimensional distance (X) measured from point B at increasing values of the non-dimensional applied displacement (Δ_A). The deformed configurations, shown on the left, have been exaggerated by a factor of 25. This is an example of type-2 debonding mechanism exhibited in Fig. 13. Note that the CZ ($\delta_c < \delta_n < \delta_f$, $0 < D < 1$) is a partially damaged region and is not traction-free.

the edge debond, and the resulting debond front propagates on continued loading (Ghatak et al., 2004). However, our plane strain analysis implies long tunnel-like debond with no undulations in the out-of-plane direction. An FE analysis of 3-D deformations by Mukherjee et al. (2016a) indicated that the internal debonding process became undulatory (wavy) when the softening stiffness of the TS relation (slope of line EF in Fig. 3) was large in comparison with the modulus to the thickness ratio of the elastomeric layer. Recalling that the spacing (λ) between the adjacent undulation peaks (Mönch and Herminghaus, 2001; Sarkar et al., 2005; Ghatak, 2006) is expected to be $\approx 3h$, the size of the CZ in a plane strain analysis must be $\gg 3h$ to capture the undulatory debonding phenomenon. Our numerical experiments reveal that the size of this CZ decreases with an increase in ϕ and a decrease in α . However,

as ϕ is increased, if the CZ size is several times the interlayer thickness determined by the combined values of both α and ϕ , the peel stress begins to oscillate with amplitudes large enough to cause wavy debonding. An example of such wavy debonding is illustrated in Fig. 10 for $\phi = 5$. Multiple debonds initiate over the CZ resulting in traction-free regions separated by portions of the damaged interface. The average spacing between these debonds is approximately $3h$, which agrees with the results of the interfacial instability (Mönch and Herminghaus, 2001; Sarkar et al., 2005; Ghatak, 2006). A comparison of our computed results for $\phi = 4$ and $\phi = 5$ suggests that the threshold value, (ϕ_c), of ϕ is in the range (4, 5). This agrees with $\phi_c \approx 4.15$ found (Mukherjee et al., 2016a) for debonding of an infinitely confined elastomeric interlayer from a rigid block pulled outwards; however, we have

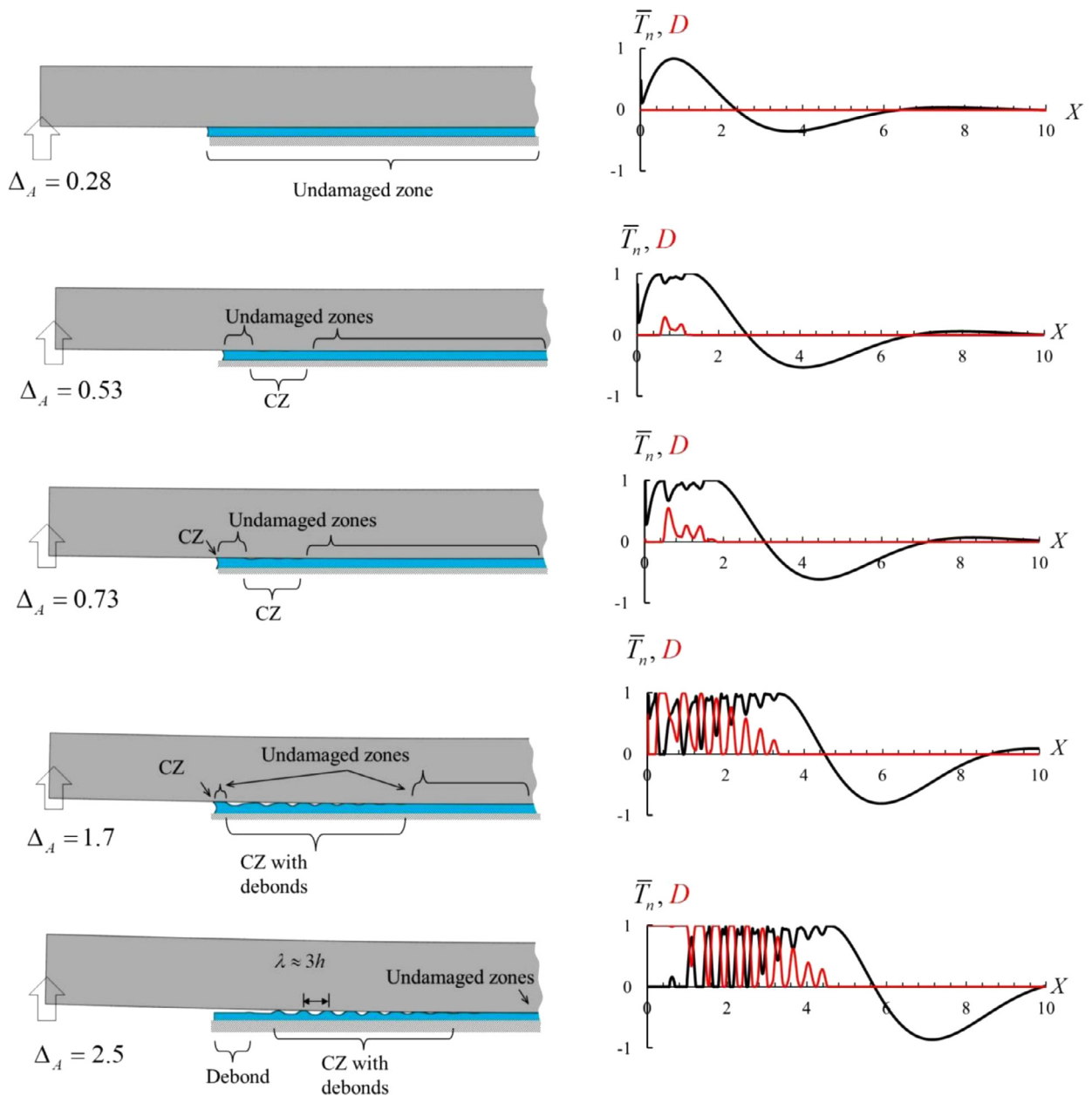


Fig. 10. For $\alpha = 100$, $\phi = 5$, distributions of the non-dimensional normal traction (\bar{T}_n) and the extent of damage (D) at the interface as a function of the non-dimensional distance (X) measured from point B at increasing values of the non-dimensional applied displacement (Δ_A). The deformed configurations, shown on the left, have been exaggerated by a factor of 25. This is an example of type-3 debonding mechanism displayed in Fig. 13. Note that the CZ ($\delta_c < \delta_n < \delta_f$, $0 < D < 1$) is a partially damaged region and is not traction-free.

not conducted sufficient number of simulations to extract the precise value of ϕ_c . The internal debonding process without wavy debonding is named type-2 and that with the softening-induced undulations is named type-3. Note that if ϕ is very large, the CZ formed at the internal peak location does not spread; instead debonding occurs and the local peel stress vanishes as illustrated in Fig. 11. The redistributed peel stress exhibits a peak at a shear-lag distance from this debond. Continued loading causes nucleation of a second internal debond which, in turn, leads to a third internal debond. This debonding mechanism is named type-4. The average spacing between the type-4 debonds is greater than $3h$ as evident from the plots of Fig. 12. A type-4 debonding mechanism differs from a type-3 mechanism in that the CZ sizes adjacent to the debonds are vanishingly small. Consequently, the predicted debonding evolution becomes sensitive to the FE mesh at large

values of ϕ (Mukherjee et al., 2016a). However, findings regarding the mechanisms of damage/debonding remain unaffected.

Presently computed predictions of the aforementioned four types of damage growth/debonding mechanisms are plotted in the $\alpha\phi$ -plane in Fig. 13. These results suggest that there is a threshold confinement, α_c , above which the peak peel stress at an interior point begins to initiate and spread damage internally. This can be explained as follows. The reduction in the load carrying capacity due to damage at the location of the internal peak begins to outweigh that due to the edge peel stress when the confinement is sufficiently large. We note that even though the peel stress has a local peak at an interior point for confinements greater than 4, the threshold confinement level, α_c , beyond which a CZ forms internally lies between 8 and 9. For the edge initiated debonding mechanism that occurs for $\alpha < \alpha_c$, the interfacial instability is not found

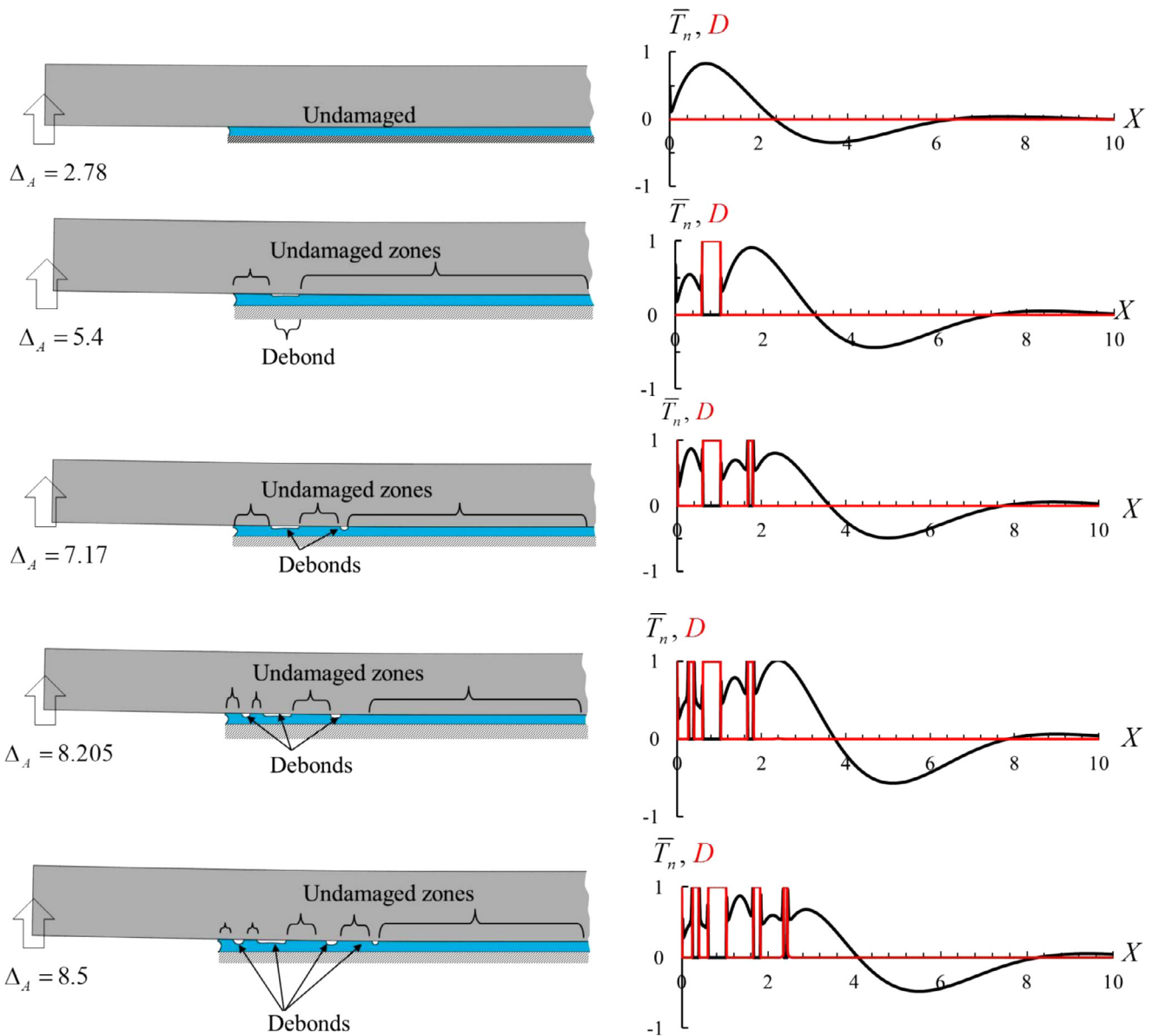


Fig. 11. For $\alpha = 100, \phi = 50$, distributions of the non-dimensional normal traction (\bar{T}_n) and the extent of damage (D) at the interface as a function of the non-dimensional distance (X) measured from point B at increasing values of the non-dimensional applied displacement (Δ_A). The deformed configurations, shown on the left, have been exaggerated by a factor of 25. This is an example of type-4 debonding mechanism evinced in Fig. 13.

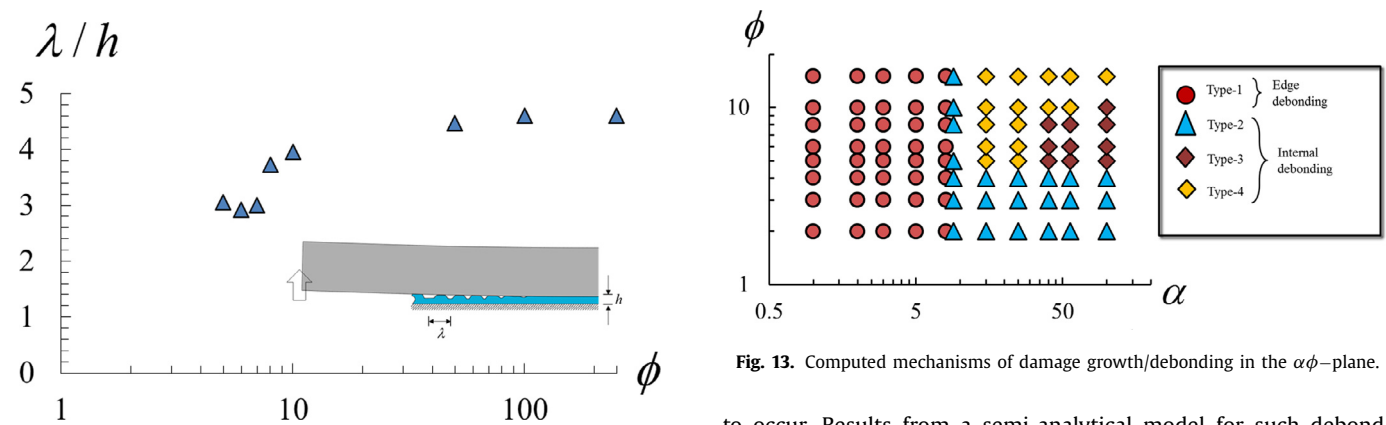


Fig. 12. On a semi-log plot, computed average spacing between the the two consecutive internal debonds normalized by the interlayer thickness as a function of ϕ when $\alpha = 100$.

Fig. 13. Computed mechanisms of damage growth/debonding in the $\alpha\phi$ -plane.

to occur. Results from a semi-analytical model for such debonding (Mukherjee et al., 2016c) show that the CZ size, d , normalized by the characteristic wavelength of undulation ($\lambda \sim 3h$), scales as $(d/\lambda) \sim (\alpha/\sqrt{\phi})$, and at $\alpha = \alpha_c$ and $\phi = \phi_c, d/\lambda < 1$. An increase

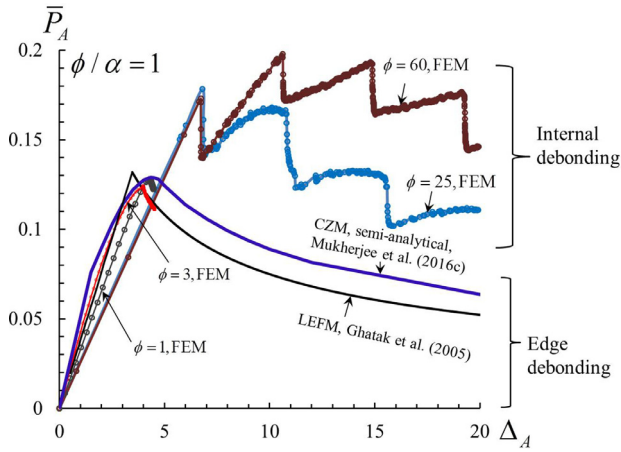


Fig. 14. Non-dimensional load vs. non-dimensional displacement for $\phi/\alpha = 1$.

in the confinement changes the debonding initiation mechanism and an increase in ϕ reduces the size of the CZ that is too small to accommodate undulations that may ensue due to the softening induced instability. This qualitatively agrees with the experimental finding of Ghatak and Chaudhury (2003) in that the confinement must exceed approximately 18 for the appearance of a fingerlike convoluted crack front. The underestimation by our analysis may be due to the assumption of plane strain deformations, and the lack of knowledge of contact conditions between the glass cover plates and the Polydimethylsiloxane (PDMS) layer used in the experiments.

4.3.2. Load-displacement curves

In terms of our normalization, the load-displacement (LD) relation found using an LEFM approach by Ghatak et al. (2005) is

$$\bar{P}_A = \frac{P_A}{D_p \beta^3 \delta_f} = \frac{6 \Delta_A}{(6 + 12A + 9A^2 + 2A^3)}$$

where the non-dimensional length, A , of a propagating crack is found from the relation $\frac{(6+12A+9A^2+2A^3)^3}{(12+46A+72A^2+56A^3+21A^4+3A^5)} = 83.9 \Delta_A^2 \frac{\alpha}{\phi}$, and P_A is the reaction force (per unit width of the plate) at point B corresponding to the crack length A . In Fig. 14 we have plotted the computed \bar{P}_A vs. Δ_A from this relation as well as that from our FE analysis of the debonding problem for $\phi = 1, 3, 25, \text{ and } 60$, $\phi/\alpha = 1$, and $A_0 = 2.83$. With increasing values of applied Δ_A , \bar{P}_A increases up to a peak value and then decreases. The nonlinearities, if any, in the initial ascending portions of these curves are attributed to the formation of the CZ near point B. For type-1 (edge initiation) debonding ($\phi = 1$ and 3), the descending portions of the LD curves are smooth. As suggested by an approximate semi-analytical model for type-1 debonding process (Mukherjee et al., 2016c), the LD curves for such debonding process depend only on the ratio ϕ/α for a given value of A_0 . The LD data computed for $\phi/\alpha = 1$ and $A_0 = 2.83$ using the semi-analytical model is included in Fig. 14. The other two computed LD curves plotted in Fig. 14 correspond to type-4 internal debonding (curves with similar features are obtained for type-2 and type-3 internal debonding). These LD histories exhibit a saw-tooth behavior which becomes more pronounced with an increase in ϕ . The LD plots for $\alpha = 100$ and $\phi = 250, 500, \text{ and } 1000$, and the corresponding deformed shapes are exhibited in Fig. 15a. These results reveal that values of δ_A corresponding to local drops in the saw-tooth behavior correlate well with those for the nucleation of internal debonds. The subsequent increase of the load with the increase in δ_A until the nucleation of the next debond is due to the retardation of the internal

debond(s) in the presence of the adjacent debond. This is reminiscent of the experimental observations of Ghatak et al. (2004) and Chung and Chaudhury (2005), during the peeling of a flexible plate from an elastomeric layer containing incisions. They observed trapping of nucleated debonds near the incisions. Our results suggest that higher values of ϕ at a given level of confinement correspond to slower propagation of debonding as evidenced by plots in Fig. 15b of the non-dimensional X-coordinate of the debond tip(s) as a function of Δ_A for $\phi = 250$ and 1000. The approximate growth rate of the 1st internal debond between its nucleation (p) and coalescence (q) with the 2nd internal debond is estimated as $(X_q - X_p)/((\Delta_A)_q - (\Delta_A)_p) = 0.0016$ for $\phi = 1000$. For $\phi = 250$, the corresponding growth rate from p' to q' equals approximately 0.0045. The increase in resistance to debond growth with increasing ϕ agrees with the saw-tooth behavior becoming more pronounced with an increase in ϕ . The growth of one debond in the presence of another adjacent internal debond controlled by the parameter ϕ has also been reported by Hill et al. (2003) in their investigation of the growth of a wedge-driven external crack in the presence of an internal void behind the crack tip. The load-displacement results begin to become mesh-sensitive for type-4 debonding mechanism owing to the CZ sizes adjacent to the debonds being vanishingly small.

In order to probe the scaling of the maximum reaction force (pull off force), numerous numerical simulations have been conducted by varying α and ϕ . The non-dimensional maximum pull-off force, \bar{P}_A^{\max} , is plotted in Fig. 16 as a function of ϕ/α . For small values of ϕ/α all data collapse on the same line for types-1, 2 and 3 debonding and agree well with predictions of a semi-analytical model of Mukherjee et al. (2016c) for type-1 debonding. The least squares fit to the data for $\phi/\alpha < \sim 2$ reveals that for types-1, 2 and 3 debonding, $\bar{P}_A^{\max} \propto (\phi/\alpha)^{0.8}$ (exponent approximate) with the constant of proportionality (~ 0.13 when $A_0 = 2.83$) dictated possibly by the non-dimensional initial overhang length, A_0 . For larger values of $\phi/\alpha (> \sim 2)$, it is found that the data for the edge-initiated debonding (type-1) satisfy the scaling $\bar{P}_A^{\max} \propto \phi/\alpha^{0.5}$ (constant of proportionality ~ 0.5) which is also obtained from an LEFM analysis (Ghatak et al., 2005).

Our computed results suggest that for type-4 debonding the maximum pull-off force begins to increase linearly for $\phi/\alpha > \sim 2$, i.e., $\bar{P}_A^{\max} \propto \phi/\alpha$ (constant of proportionality ~ 0.7 when $A_0 = 2.83$), although the computed data points at different confinement levels suggest additional weak dependence on α . We have summarized in Table 1 the collective role of the confinement and the interfacial adhesion on the non-dimensional pull-off force (in our numerical experiments the confinement was varied within the range $1 < \alpha < 100$ and the adhesion parameter within $0.01 < \phi < 500$). For ease of interpretation, the dependence of the dimensional force on the plate flexural rigidity, the interlayer thickness, the interlayer modulus, the peak traction (T_c) and the fracture energy (\mathcal{G}_c) is also included. These results suggest that the pull-off force depends on T_c more strongly than on other parameters for small values of the adhesion parameter. For small values of the confinement and large values of the adhesion parameter, (small confinement (adhesion) is defined as one for which $\alpha < \sim 9$ ($\phi/\alpha < \sim 2$)) the results can be described by the LEFM - based analysis; the pull-off force then strongly depends on the geometric and the material parameters, and on \mathcal{G}_c but does not depend on the peak traction. For large value of the confinement and large values of the adhesion parameter, the pull off force scales with T_c , shows weak dependence on the plate rigidity, and depends on the thickness and the modulus of the interlayer in a way opposite to that for less confined interlayers and exhibits no dependence on the fracture energy. These dependencies can potentially be used to find values of the TS parameters from the pull-off force data obtained in suitably designed experiments.

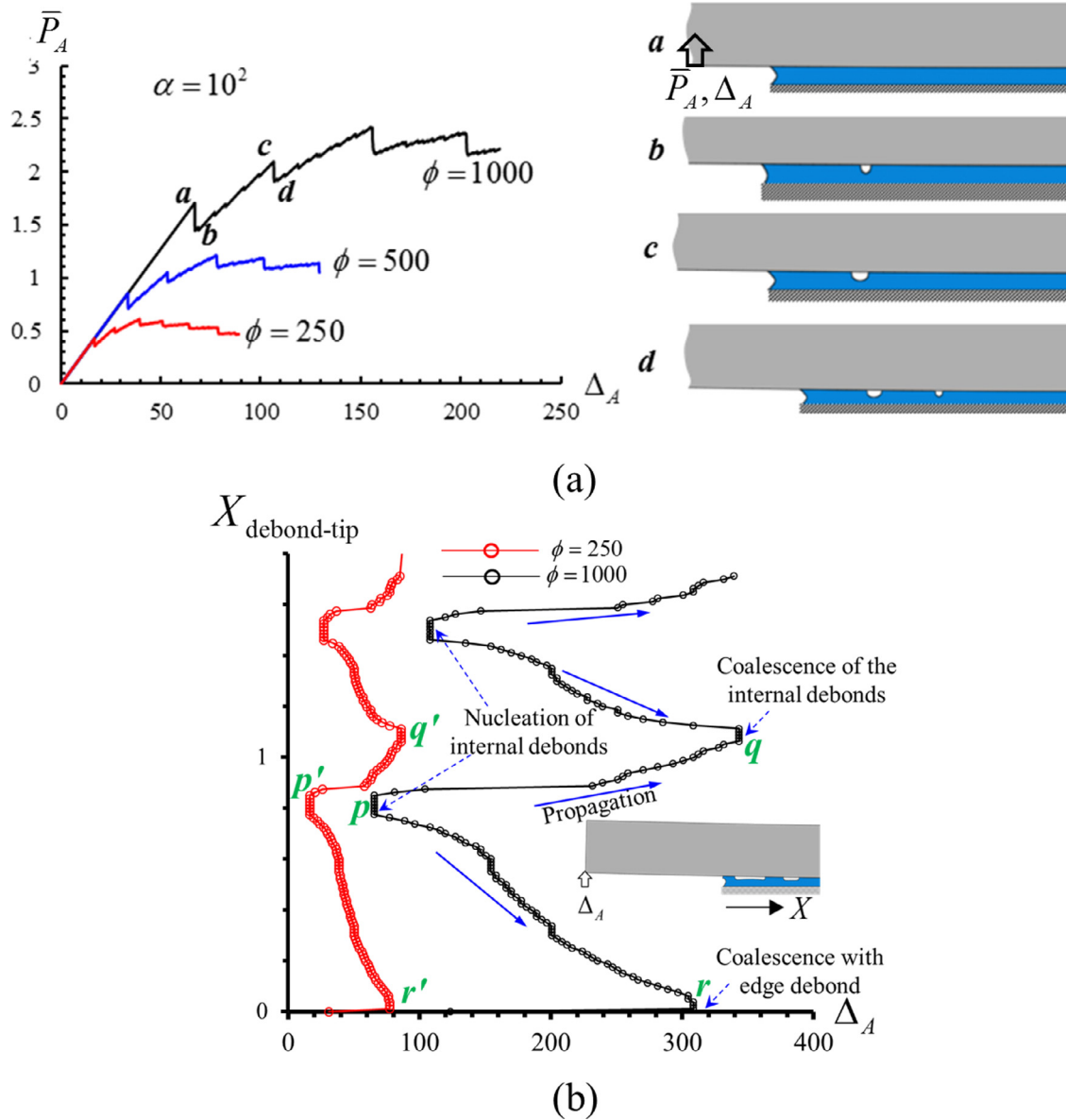


Fig. 15. (a) Non-dimensional load versus non-dimensional tip-displacement plots for $\alpha = 100$ and three values of ϕ . Deformed shapes (exaggerated by a factor of 20) corresponding to points a, b, c and d are included in the right figure; (b) Plots of X -coordinate of the debond tip as a function of the applied non-dimensional tip-displacement for $\phi = 250$ and 1000 .

Table 1
Effect of confinement and adhesion on the pull-off force.

Confinement, α	Adhesion, ϕ	Classification of damage/debonding initiation	The non-dimensional pull off force, \bar{P} , is proportional to	The dimensional pull off force, P , is proportional to
Small	Small	Type-1	$(\phi/\alpha)^{0.8}$	$D_p^{\frac{2}{3}} \mu^{-\frac{1}{30}} h^{\frac{1}{10}} \mathcal{G}_c^{\frac{1}{3}} T_c^{\frac{2}{3}}$ (exponents approximate)
Large	Small	Type-2,3		
Small	Large	Type-1	$(\phi/\alpha)^{0.5}$	$D_p^{\frac{1}{3}} \mu^{\frac{1}{6}} h^{-\frac{1}{2}} \mathcal{G}_c^{\frac{1}{2}}$
Large	Large	Type-4	ϕ/α	$D_p^{\frac{1}{3}} \mu^{-\frac{1}{6}} h^{\frac{1}{2}} T_c$ (exponents approximate)

4.3.3. Limitations

Experimental findings (Ghatak and Chaudhury, 2003; Ghatak et al., 2004) and simulations of 3-D deformations (Biggins et al., 2013; Mukherjee et al., 2016a) suggest that the adhesion-induced instability triggers oscillations in the out-of-plane (the y -) direction resulting in a fingerlike debonding front. However, the assumption of plane strain deformations, and hence no variation in the out-of-plane direction, forces the instability to develop in the x -direction. Instabilities in both the x - and the y - directions have been

experimentally observed for very large values of the confinement ($\alpha = 67$) by Ghatak et al. (2000). A plane-strain assumption, in general, fails to predict details of pattern formation during the debonding process because the inhomogeneity in the out-of-plane traction distribution due to the presence of traction-free surfaces and anticlastic bending of the plate lead to (i) undulatory debonding in the y -direction and (ii) multiple debonds rather than a tunnel-like debond assumed for plane-strain deformations. This is confirmed by comparing results of analyzing 3-D deformations

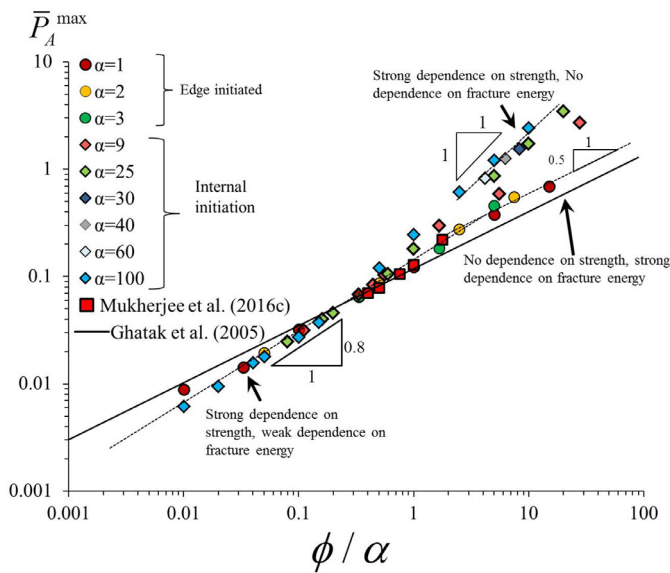


Fig. 16. Dependence of the non-dimensional pull-off force on the non-dimensional number ϕ/α .

with and without restraining the y -displacement of points on the lateral surfaces of the plate. Nevertheless, results presented here are useful for predicting the onset of different types of debonding in a semi-infinite geometry as a function of the confinement and the CZM parameters. Results for a few 3-D problems included in Appendix C support conclusions drawn from the analysis of plane strain deformations.

Recalling that the present problem involves a mixed-mode loading (Suo and Hutchinson, 1989; Hutchinson and Suo, 1991; Li et al., 2004), one restricting assumption of the present work is that of the interfacial interaction being much weaker in the normal direction than that in the tangential direction. However, as supported by results of an example problem included in Appendix D, the debonding mechanisms are qualitatively unchanged even when similar interaction is considered in both the normal and the tangential directions.

4.4. Debonding at both interfaces of the interlayer

Industrial fabrication of soft bio-implants such as ophthalmic lenses often involves the release of an elastomeric interlayer sandwiched between two molds from a desired mold interface by mechanically prying open one of the molds (Larsen, 1987). A potential problem, when the interfaces have identical adhesion, is the occurrence of debonding at the undesirable interface and/or at both interfaces, resulting possibly in a bridge of the interlayer suspended between the two molds. This renders the interlayer susceptible to tearing failure. Computed results of some additional numerical experiments are presented that may help design potential strategies for engineering a desired release mechanism.

The configuration analyzed is schematically shown in Fig. 17a, and values of various parameters are given in the Figure legend. It is similar to that depicted in Fig. 4 except that the lower adherend is also made of an isotropic and homogeneous linear elastic material and the two adherends have the same overhang length of 2.83 mm¹². Referring to Fig. 17a, the edge of the upper flexible plate is monotonically displaced upwards and the three displacement components of points on the bottom surface of the lower plate are set

¹² 4-node square elements of dimensions 0.1 mm \times 0.1 mm and 0.025 mm \times 0.025 mm have been used to discretize the molds (CPE4 elements) and the interlayer (CPE4H elements), respectively.

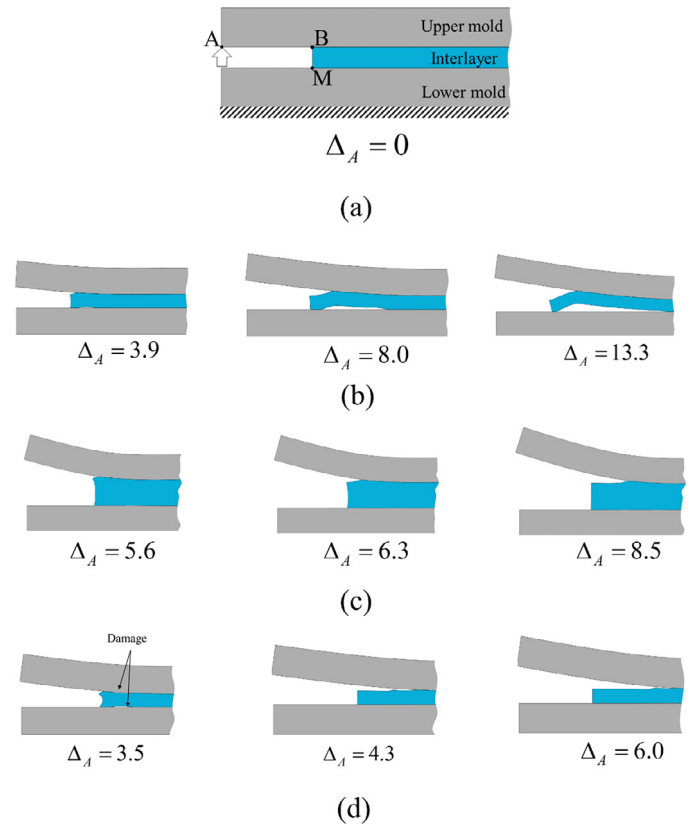


Fig. 17. (a) The configuration analyzed; snapshots (exaggerated by a factor of 100) of the interfacial debonding for (b) $\alpha = 8$, (c) $\alpha = 2$ and (d) $\alpha = 10$, and the same values of the TS parameters at both interfaces corresponding to $T_c = 0.04$ MPa and $\phi = 4$ when vertical displacement is monotonically increased at point A. The thickness and the total length of each plate in the numerical simulations are taken to be 1 mm and 50 mm, respectively. Both adherends have Poisson's ratio of 0.3. Values of other parameters are: $a_0 = 2.83$ mm, $\beta^{-1} = 1$ mm and $K_e = 10^6$ N/mm³.

equal to zero to simulate the fixed base. To be consistent with the work reported in the previous section, we assume that the interfacial damage dominantly in tension.

As the upper plate is loaded, the asymmetry of materials, loading and boundary conditions on the two adherends causes a shearing bias at point B in Fig. 17a, that results in opening at the upper interface near point B due to peeling-shearing coupling. We recall that when the lower interface has infinite strength, the confinement has to exceed a threshold value for debonding to initiate at an interior point due to the peak stress there. Before damage initiation the computed distributions of the peel stress at the two interfaces reveal that the peel stresses are nearly identical at the two interfaces except at points close to the corners. Due to the opening bias at point B, it is speculated that a lower threshold confinement level is needed for the internal debonding to ensue at the lower interface than that at the upper interface. When the two interfaces have the same strength, the simulation results shown in Fig. 17b–d indicate that there is a range of confinement values for which internal debonding initiates at the lower interface with the edge crack initiated at the upper interface. For $\alpha = 8$ the internal debond does not nucleate at the upper interface but nucleates and grows at the lower interface thereby causing an undesirable bridge of the interlayer suspended between the two adherends as shown in Fig. 17b. One way to mitigate this is to reduce the level of confinement so that the peak peel stress at interior points is small. The simulation results for $\alpha = 2$ plotted in Fig. 17c support this. However, for sufficiently confined interlayers, such as that shown in Fig. 17d for $\alpha = 10$, damage may occur at interior points

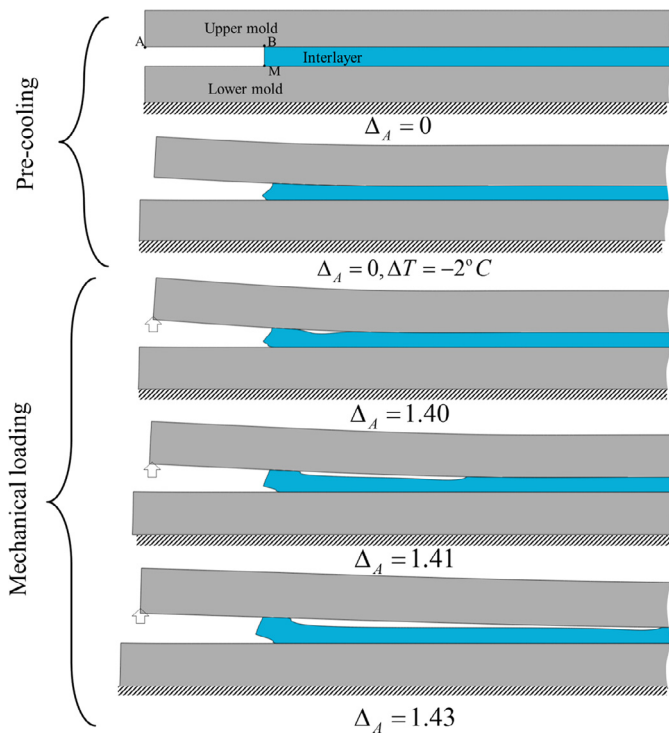


Fig. 18. Snapshots of debond growth (exaggerated by a factor of 100) when the assembly is pre-cooled homothermally by -2°C followed by a vertical displacement applied at point A while the displacement components at the bottom surface of the lower mold equal zero. The coefficients of thermal expansion are assumed to be $7 \times 10^{-5}/^\circ\text{C}$ and $6 \times 10^{-4}/^\circ\text{C}$ for the two molds and the interlayer materials, respectively. The pre-cooling stage is simulated by inputting $\Delta T = -2^\circ\text{C}$ and no thermal effects are simulated for the mechanical loading stage. These results are for the confinement $\alpha = 8$ and equal values of the TS parameters at both interfaces corresponding to $T_c = 0.04$ MPa and $\phi = 4$. Both adherends have Poisson's ratio of 0.3. Values of other parameters are: $a_0 = 2.83$ mm, $\beta^{-1} = 1$ mm and $K_e = 10^6$ N/mm³.

on both interfaces at locations of peak stresses. Continued loading causes the lower interface CZ to become shielded (Hutchinson, 1987) by the growth of the CZ on the upper interface. These observations suggest that an improper level of confinement may result in an erratic debonding process. In practical situations, however, the choice of tailoring the confinement by tuning the mold flexibilities may be limited. As was suggested by Feurer (1983), thermal pre-conditioning can be used to bias debonding to a desired interface. For example, pre-cooling (values listed in the Figure legend) the assembly before mechanically pulling the upper mold for $\alpha = 8$ causes the internal debond to initiate and grow at the upper interface as can be seen from the results exhibited in Fig. 18. Due to the mismatch in the coefficients of thermal expansion of the molds and the interlayer and the associated bending of the flexible upper mold, the peel stress is compressive near the upper interface corner point B and tensile at the lower interface corner point M. As a result of the opening bias at the lower interface corner, the edge debond initiates at M and the internal debonding nucleates and grows at the upper interface. These debonding characteristics remain unchanged upon refining the FE mesh. Since shear interaction may play an important role in determining preferential debonding when two interfaces in a three-layer sandwich structure are equally weak, only mode-I debonding considered here may not have provided an accurate assessment of the tearing phenomenon. A more detailed investigation (Mukherjee, 2016) of tailoring the confinement, the ratio of the elastic moduli of the two adherends, and the thermal pre-conditioning to cause preferential debonding will be reported elsewhere (Mukherjee et al., 2016d).

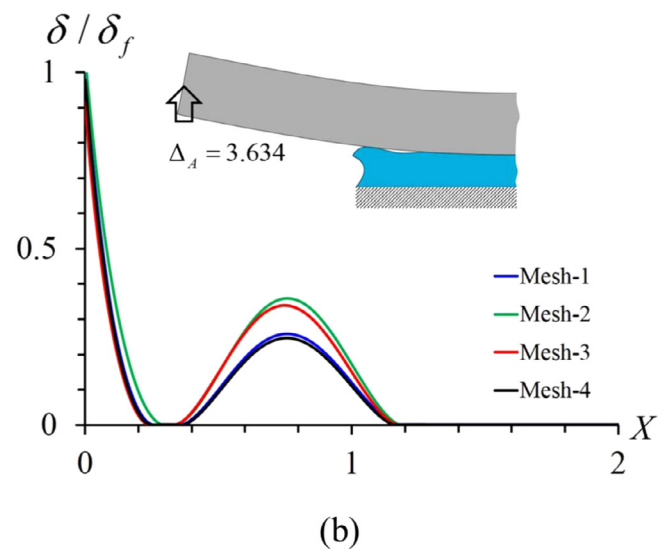
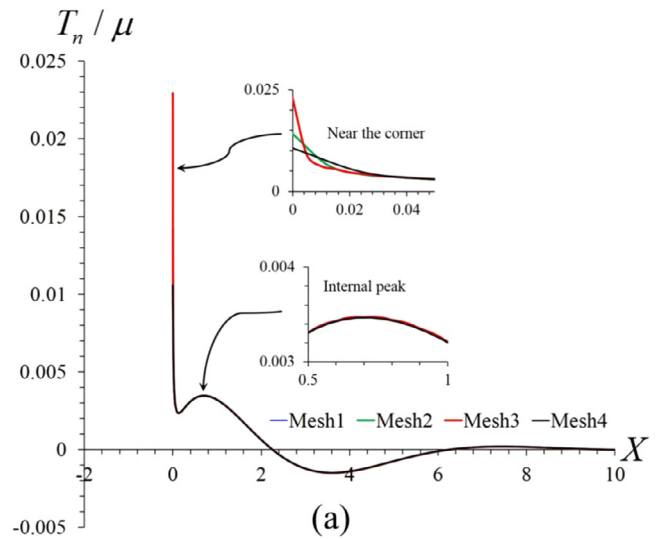


Fig. A1. For $\alpha = 8$, sensitivity to the FE mesh of (a) distribution of the peel stress at the interface yet to damage when $\delta_A = 1$ μm , and (b) distribution of the contact opening when $\phi = 4$, $\Delta_A = 3.634$. The inset shows the exaggerated (by a factor of 20) deformed configuration.

5. Conclusions

We have studied interfacial debonding of a flexible plate from an elastomeric layer firmly bonded to a rigid substrate by using a cohesive zone model (CZM) and analyzing plane strain infinitesimal deformations of the linear elastic flexible plate and the elastomeric layer by using the finite element commercial software, ABAQUS/Standard. The effects of the following two dimensional parameters have been investigated

- Confinement parameter, $\alpha = (D_p/\mu h^3)^{1/3}$, relating the flexural rigidity, D_p , of the plate and the shear modulus, μ ($=$ (Young's modulus, E)/3), and thickness, h , of the interlayer. This parameter was shown to be important by Ghatak and Chaudhury (2003), Adda-Bedia and Mahadevan (2006) and Vilmin et al. (2009).
- CZM/adhesion parameter, $\phi = T_c^2 h/\mathcal{G}_c E$, relating the peak traction T_c for damage initiation at an interface point and the fracture energy \mathcal{G}_c in the CZM traction-separation (TS) relation.

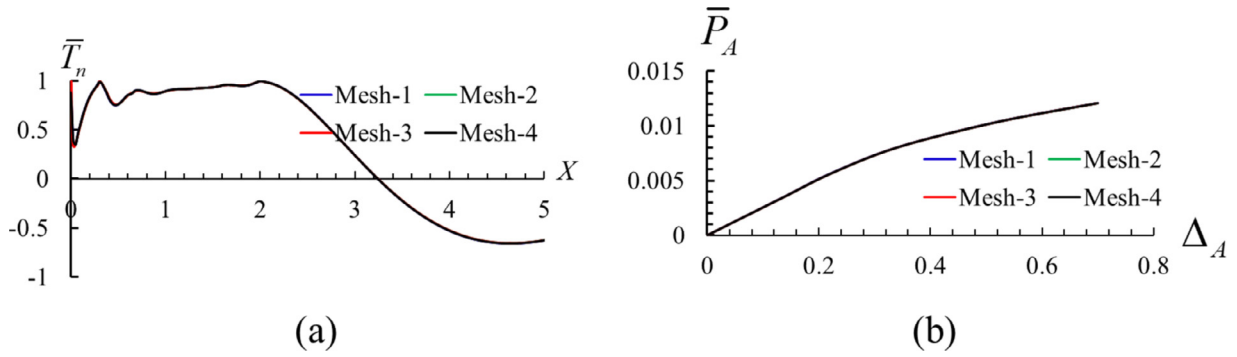


Fig. A2. For $\alpha = 100$ and $\phi = 4$, sensitivity to the FE mesh of (a) the non-dimensional peel stress distribution for $\Delta_A = 0.7$, and (b) the non-dimensional load-displacement variation until $\Delta_A = 0.7$. This represents a type-2 debonding as illustrated in Fig. 9.

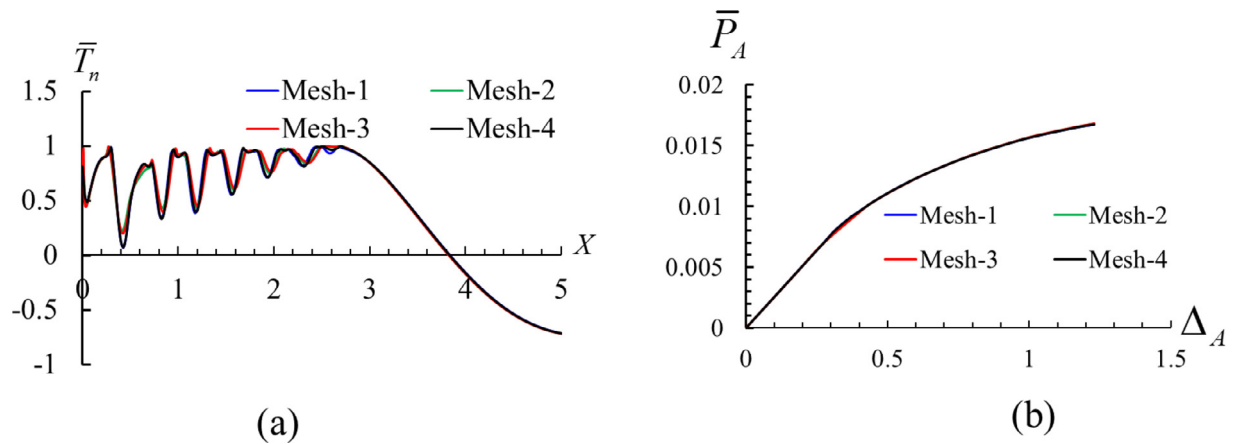


Fig. A3. For $\alpha = 100$ and $\phi = 5$, sensitivity to the FE mesh of (a) the non-dimensional peel stress distribution for $\Delta_A = 1.2$, and (b) the non-dimensional load-displacement variation until $\Delta_A = 1.2$. This represents type-3 debonding as illustrated in Fig. 10.

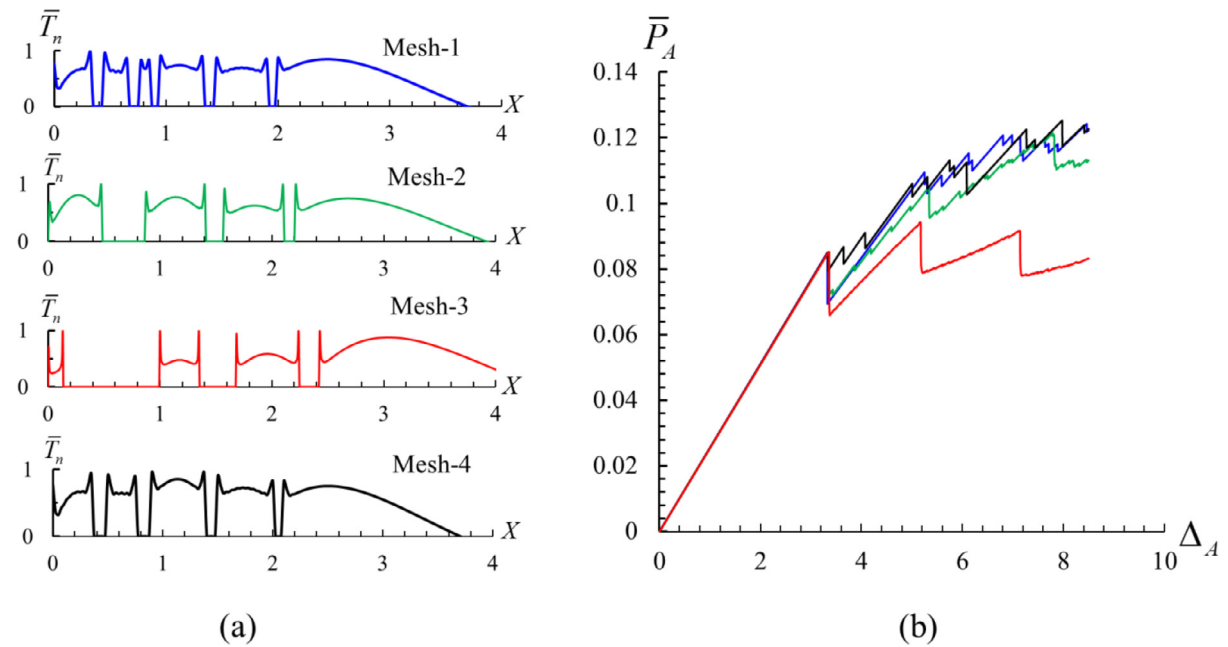


Fig. A4. For $\alpha = 100$ and $\phi = 50$, sensitivity to the FE mesh of (a) the non-dimensional peel stress distribution for $\Delta_A = 8.5$, and (b) the non-dimensional load-displacement variation until $\Delta_A = 8.5$. This represents a type-4 debonding as illustrated in Fig. 11. As discussed in Section 4, the dip in the load-displacement plot corresponds to the initiation of internal debonding.

Mukherjee et al. (2016a) have elucidated the importance of this parameter for wavy interfacial debonding of a rigid adherend pulled outwards from an elastomeric interlayer.

Results of numerical simulations have been plotted on the $\alpha\phi$ -plane to identify values of α and ϕ for four different interfacial debonding types. For confinement levels less than a threshold value (~ 9), damage at the interface between the interlayer and the deformable plate initiates at the edge, forms a cohesive zone (CZ), and leads to debonding which propagates with a CZ at its front. When confinement exceeds the threshold value, the damage in addition to occurring at the edge initiates at an internal interface point located at dimensionless distance $\beta^{-1} \sim (\mu/D_p h^3)^{-1/6}$ from the edge, which is proportional to the characteristic stress decay distance (one can also think of this as a shear-lag distance). For such interlayers a wavy debonding occurs when the adhesion parameter exceeds a critical value. However, for large values of ϕ dictated by the confinement two adjacent nucleated debonds are separated by a perfectly bonded region rather than by a portion of the damaged interface. The spacing, λ , between the internal debonds scales with the interlayer thickness.

The non-dimensional pull-off force is found to increase with the quantity ϕ/α and depend on the debonding type.

For an elastomeric layer sandwiched between a flexible adherend and a rigid substrate with the two interfaces having identical TS relations, it was found that for confinement not in the appropriate range separation can occur at both interfaces resulting in an erratic release process and leading to bridging which can result in undesirable tearing of the interlayer.

Acknowledgments

The authors are grateful to the two anonymous reviewers for providing constructive comments and suggestions on an earlier version of the paper that have improved upon the presentation of the work. They also thank the department of Biomedical Engineering and Mechanics at Virginia Tech for the use of its facilities and the Macromolecules and Interfaces Institute, Virginia Tech, for fostering interdisciplinary research in the adhesion area.

Appendix A

Included here are the sensitivities of the interfacial normal traction and the load-displacement plots to four FE meshes listed in Table A1. In Fig. A1a, we have plotted the distribution of the peel stress at the interface which is yet to damage. It is clear that the peel stress distribution is insensitive to the FE mesh used except for the discretization close to the corner point B. However, the interfacial damage type is unaltered as evinced by the plot of the contact opening shown in Fig. A1b. Figs. A2–A4 show distributions of the non-dimensional peel stress upon damage initiation at the interface (a) and the non-dimensional load-displacement variations

Table A1
The FE meshes used^a.

FE meshes	Dimensions in mm of an element of the interlayer	Dimensions in mm of an element of the plate
Mesh-1	0.025 × 0.025	0.1 × 0.1
Mesh-2	0.0125 × 0.0125	0.1 × 0.1
Mesh-3	Height: 0.0125, width: graded from 0.05 at the farthest end to 0.005 near point B.	0.1 × 0.1
Mesh-4	0.025 × 0.025	0.05 × 0.05

^a Results reported in this paper were obtained with FE mesh-2, unless mentioned otherwise.

(b) for the debonding types-2, 3 and 4, respectively. As was reported in Mukherjee et al. (2016a), one can observe that the results are more sensitive to the changes in the FE mesh for a large value of ϕ as compared to those for a small value of ϕ . Nonetheless, our conclusions about the type of debonding and the scaling of the pull-off force remain unaffected on refining further the FE mesh 2. The load-displacement curves depicted in Fig. A4 are close to each other for FE meshes 3 and 4 but differ slightly from that for FE mesh 2 for which results are reported in the paper.

Appendix B

The work done by the external force should equal the sum of the increase in the strain energy of the system, the energy lost due to interfacial damage/debonding, and the energy loss due to the damage stabilization (viscous regularization) option used in ABAQUS. For one example problem for which values of variables are listed in the Figure label, the evolutions of these energies are plotted in Fig. B1a. It is clear that the energy balance is satisfied with the maximum error of $\sim 6\%$. Also included in Fig. B1b are plots of the interfacial traction components at $\delta_A = 15 \mu\text{m}$.

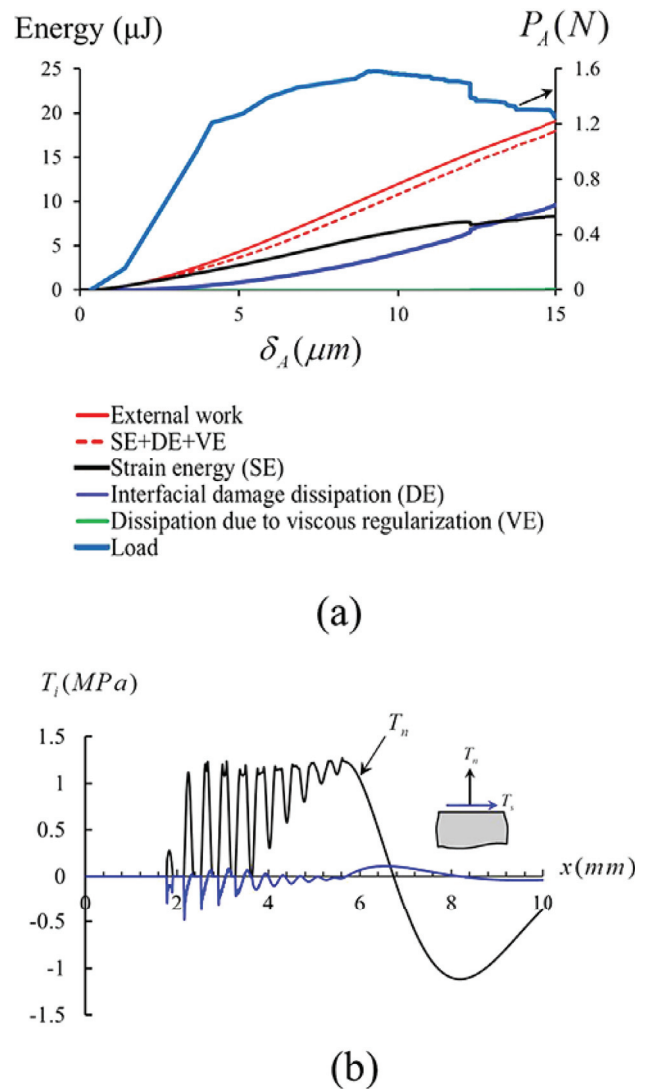


Fig. B1. (a) Computed energy histories for $\alpha = 100$ and $\phi = 5$. The out-of-plane dimension (width) is taken to be 1 mm when computing the total energy. As discussed in Section 4, the dip in the load-displacement plot corresponds to the initiation of internal debonding. (b) Distributions of interfacial traction components at $\delta_A = 15 \mu\text{m}$.

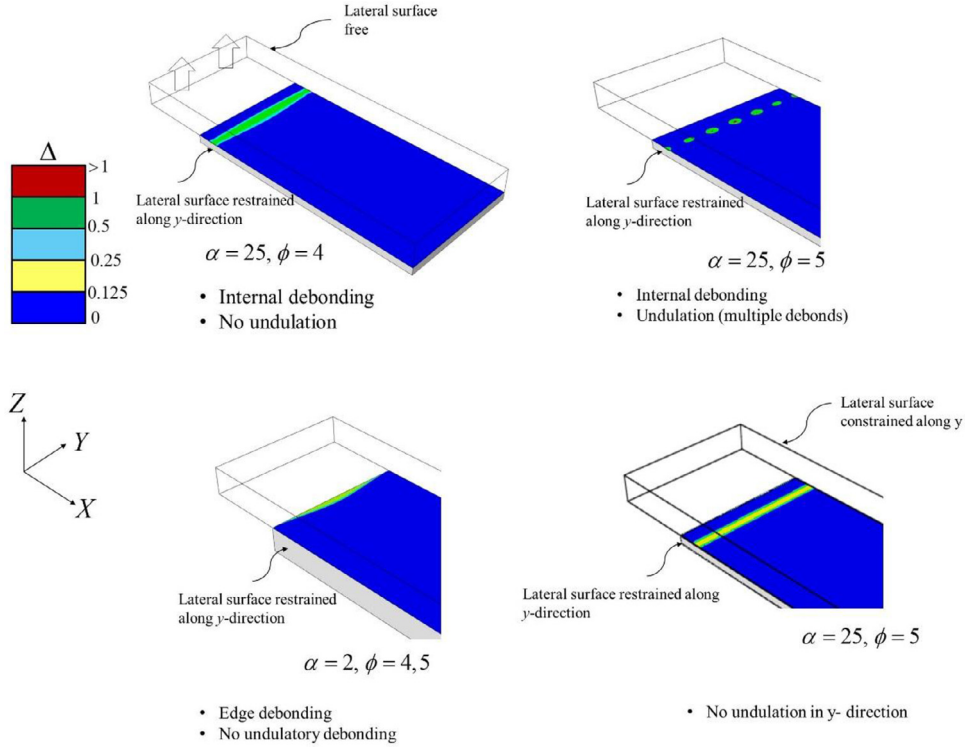


Fig. C1. Snapshots of the interfacial dimensionless contact opening for $\phi = 4$ and 5 and confinement $\alpha = 25$ and 2, when the lateral surfaces of the interlayer are prevented to deform in the y-direction but those of the plate are free. The bottom right figure corresponds to $\alpha = 25$ and $\phi = 5$ when the lateral surfaces of both the plate and the interlayer are restrained in the y-direction.

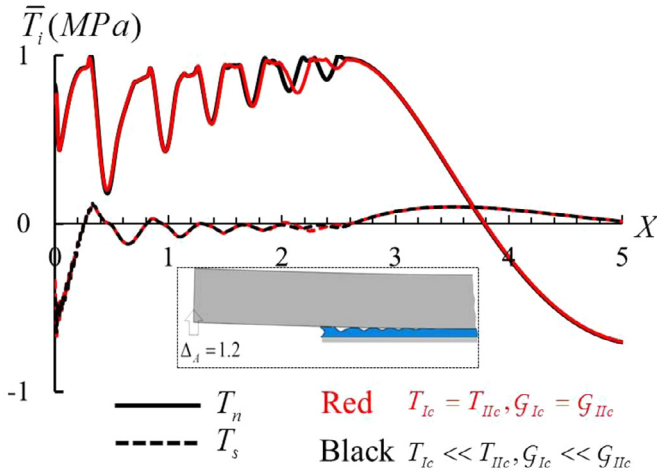


Fig. D1. Distributions of the interfacial peel stress for $\alpha = 100, \phi = 5$ and $\Delta_A = 1.2$ when the normal interaction is much weaker than the shear interaction and when both interactions are equally weak. The deformed shape is exaggerated by a factor of 20 for visualization.

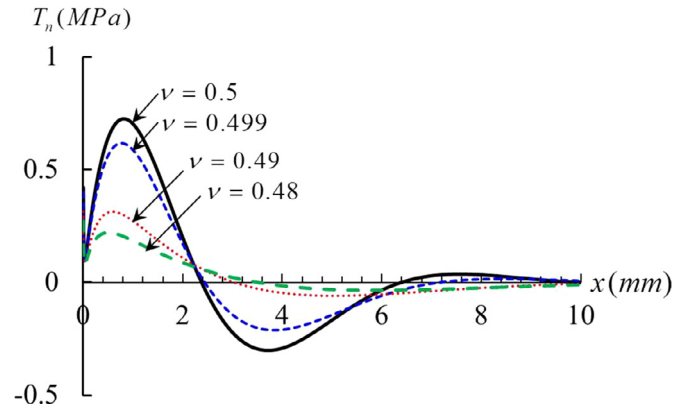


Fig. E1. Distributions of the interfacial peel stress for $\alpha = 100$ and four indicated values of Poisson's ratio of the interlayer when the applied displacement is $1 \mu\text{m}$. These results are for an undamaged interface.

Appendix C

Three-dimensional (3-D) deformations have been studied for four cases to check if predictions of the debonding types on the $\alpha\phi$ -plane from analysis of plane strain deformations agree with those from the analysis of 3-D deformations. The out-of-plane width (y-direction) and the length (x-direction) of the assembly are assumed to be 5 mm and 12.83 mm, respectively, and the thickness is chosen to get the desired degree of confinement. In ABAQUS terminology, the plate and the interlayer are discretized using C3D8R and C3D8H elements, respectively. Brick elements of dimensions $0.025 \text{ mm} \times 0.025 \text{ mm} \times 0.025 \text{ mm}$, and $(h/5)$ (thickness) $\times l$ (length) $\times 0.025 \text{ mm}$ (width) are used to discretize the plate and the interlayer, respectively, where l is the element length decreasing from 0.075 mm at the farthest end ($x = 12.83$

The computed energy dissipation due to damage for $\delta_A = 15 \mu\text{m}$ differed by $\sim 6\%$ from that found using the equation, $DE = G_c a + \int_{l_{CZ}} (G_c - \frac{T_c^2}{4G_c} (\frac{2G_c}{T_c} - \delta(x))^2) dx$. Here the integrand represents, for $K_e > > 1$, the area under the portion of the TS curve traced by a point in the CZ up to the contact opening of δ ($> \delta_c$ and $< \delta_f$) and the integral is computed using the Trapezoidal rule, a is the total length of the interfacial debond, l_{CZ} the total length of the CZ, and $\delta(x)$ the contact opening at a point in the CZ. It ensures that DE is computed well in ABAQUS.

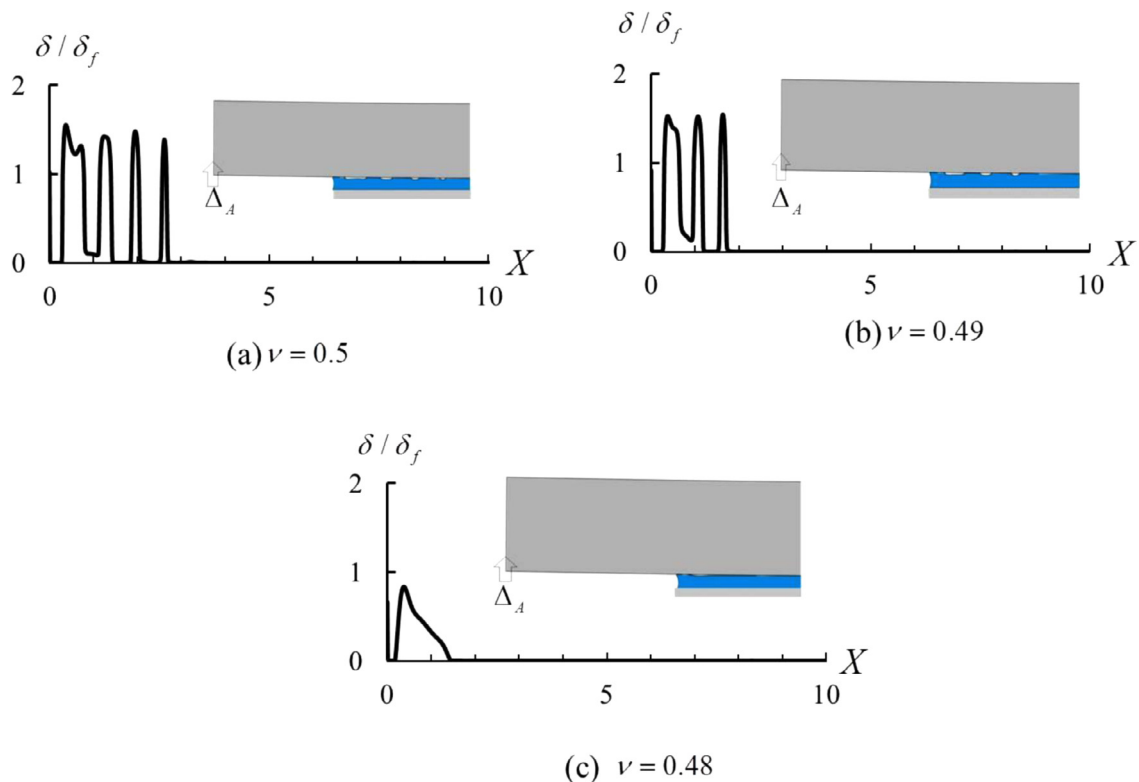


Fig. E2. Distributions of the dimensionless contact opening for $\alpha = 100$, $\phi = 10$ and at $\Delta_A = 3.45$ for (a) $\nu = 0.5$, (b) $\nu = 0.49$, and (c) $\nu = 0.48$. The deformed shapes are exaggerated by a factor of 200 for visualization.

mm) of the interlayer to 0.03 mm near the free edge. Results of simulations of 3-D deformations are depicted in Fig. C1. For $\alpha = 25$, multiple internal openings appear (type-3) along the y -direction for $\phi = 5$ whereas only a tunnel-like opening (type-2) occurs for $\phi = 4$. For $\alpha = 2$, debonding initiates from the edge and undulations are not found to occur for both values of ϕ (type-1). These simulations support the conclusions drawn from the analysis of plane strain deformations in the xz -plane. The above simulations of 3D deformations were conducted by setting to zero the y -displacements of nodes on the lateral surfaces of the elastomeric layer but not those of the plate. The bottom right figure exhibits a snapshot of the computed contact opening for $\alpha = 25$ and $\phi = 5$ when the lateral surfaces of the plate were also restrained in the y -direction. With no y -direction variations in the deformations, a tunnel-like debonding was predicted.

Appendix D

Here we include one example problem in which the interface is considered to be equally weak in both normal and tangential directions. Fig. D1 shows distribution of the interfacial peel stress and tangential traction for a highly confined interlayer, $\alpha = 100$, and for the adhesion parameter, $\phi = 5$. Similar to what is predicted under the assumption of relatively much stronger shear interaction, a type-3 debonding mechanism is predicted.

Following the suggestion made by an anonymous reviewer, we checked the computed energy balance for this problem. A discrepancy of $\sim 6\%$ was found for both cases: dominant normal interaction and equal interactions in both normal and tangential directions. This finding rules out the likelihood of our assumption of dominant normal interaction causing the discrepancy in the energy balance.

Appendix E

As suggested by a reviewer, we include here computed results for some additional numerical experiments conducted to probe sensitivity of our predictions to small deviations from incompressibility of the interlayer. CPE4 elements were used to mesh the interlayer. Distributions of the peel stresses at an undamaged interface, at the same level of confinement, $\alpha = 100$, and applied displacement, $1 \mu\text{m}$ are shown in Fig. E1 for four values of Poisson's ratio of the interlayer. These results suggest that the internal peak stress and the area over which it is distributed decrease with an increase in the compressibility of the interlayer.

Fig. E2 shows the distributions of the dimensionless contact opening when damage is allowed to occur at the interface for $\alpha = 100$, and $\nu = 0.5, 0.49$ and 0.48 , with the TS parameters so chosen that $\phi = 10$. The results are plotted at the dimensionless applied displacement $\Delta_A = 3.45$. While internal debonding is predicted for all three cases due to sufficiently large confinement, the number of internal debonds (type-4) is largest for the perfectly incompressible case. These results suggest that the introduction of slight compressibility of the interlayer relieves the constraint imposed on the interlayer and therefore, the internal damage decreases.

These results and the findings of Shenoy and Sharma (2001) about the interfacial pattern formation for compressible films suggest that the predicted map of debonding mechanisms (such as that shown in Fig. 13) is affected by the compressibility of the interlayer. A detailed analysis is not undertaken in the present work.

References

- Adda-Bedia, M., Mahadevan, L., 2006. Crack-front instability in a confined elastic film. *Proc. R. Soc. A* 462 (2075), 3233–3251.
- Anderson, G., DeVries, K., Williams, M., 1974. Mixed mode stress field effect in adhesive fracture. *Int. J. Fract.* 10 (4), 565–583.

- Anderson, G.P., Bennett, S.J., DeVries, K.L., 1977. Analysis and Testing of Adhesive Bonds.
- Anderson, T.L., 2005. Fracture Mechanics: Fundamentals and Applications. CRC press.
- Bao, G., Suo, Z., 1992. Remarks on crack-bridging concepts. *Appl. Mech. Rev.* 45 (8), 355–366.
- Barenblatt, G.I., 1962. The mathematical theory of equilibrium cracks in brittle fracture. *Adv. Appl. Mech.* 7 (1), 55–129.
- Biggins, J.S., Saintyves, B., Wei, Z., Bouchaud, E., Mahadevan, L., 2013. Digital instability of a confined elastic meniscus. *Proc. Natl. Acad. Sci.* 110 (31), 12545–12548.
- Bogy, D.B., 1968. Edge-bonded dissimilar orthogonal elastic wedges under normal and shear loading. *J. Appl. Mech.* 35 (3), 460–466.
- Camanho, P.P., Davila, C., De Moura, M., 2003. Numerical simulation of mixed-mode progressive delamination in composite materials. *J. Compos. Mater.* 37 (16), 1415–1438.
- Chadegani, A., Batra, R.C., 2011. Analysis of adhesive-bonded single-lap joint with an interfacial crack and a void. *Int. J. Adhes. Adhes.* 31 (6), 455–465.
- Chung, J.Y., Chaudhury, M.K., 2005. Roles of discontinuities in bio-inspired adhesive pads. *J. R. Soc. Interface* 2 (2), 55–61.
- Creton, C., Hooker, J., Shull, K.R., 2001. Bulk and interfacial contributions to the debonding mechanisms of soft adhesives: extension to large strains. *Langmuir* 17 (16), 4948–4954.
- Creton, C., Lakrout, H., 2000. Micromechanics of flat-probe adhesion tests of soft viscoelastic polymer films. *J. Polym. Sci. Part B: Polym. Phys.* 38 (7), 965–979.
- Crosby, A.J., Shull, K.R., Lakrout, H., Creton, C., 2000. Deformation and failure modes of adhesively bonded elastic layers. *J. Appl. Phys.* 88 (5), 2956–2966.
- Dillard, D., 1989. Bending of plates on thin elastomeric foundations. *J. Appl. Mech.* 56 (2), 382–386.
- Dugdale, D., 1960. Yielding of steel sheets containing slits. *J. Mech. Phys. Solids* 8 (2), 100–104.
- Dundurs, J., 1969. Discussion: “Edge-bonded dissimilar orthogonal elastic wedges under normal and shear loading” (Bogy, DB, 1968, ASME J. Appl. Mech., 35, pp. 460–466). *J. Appl. Mech.* 36 (3), 650–652.
- Feurer, B., 1983. Method for molding contact lenses using microwave energy. U.S. Patent No. 4,390,482.
- Gent, A., 1994. Compression of rubber blocks. *Rubber Chem. Technol.* 67 (3), 549–558.
- Geubelle, P.H., Baylor, J.S., 1998. Impact-induced delamination of composites: a 2D simulation. *Compos. Part B* 29 (5), 589–602.
- Ghatak, A., 2006. Confinement-induced instability of thin elastic film. *Phys. Rev. E* 73 (4), 041601.
- Ghatak, A., Chaudhury, M.K., 2003. Adhesion-induced instability patterns in thin confined elastic film. *Langmuir* 19 (7), 2621–2631.
- Ghatak, A., Chaudhury, M.K., Shenoy, V., Sharma, A., 2000. Meniscus instability in a thin elastic film. *Phys. Rev. Lett.* 85 (20), 4329.
- Ghatak, A., Mahadevan, L., Chaudhury, M.K., 2005. Measuring the work of adhesion between a soft confined film and a flexible plate. *Langmuir* 21 (4), 1277–1281.
- Ghatak, A., Mahadevan, L., Chung, J.Y., Chaudhury, M.K., Shenoy, V., 2004. Peeling from a biomimetically patterned thin elastic film. *Proc. R. Soc. Lon. Series A* 460 (2049), 2725–2735.
- Gowrishankar, S., Mei, H., Liechti, K.M., Huang, R., 2012. A comparison of direct and iterative methods for determining traction-separation relations. *Int. J. Fract.* 177 (2), 109–128.
- Hibbitt, K., Sorensen, 2012. ABAQUS/CAE User's Manual. Hibbitt, Karlsson & Sorensen, Incorporated.
- Hill, J., Bennison, S., Klein, P., Foulk, J., Jagota, A., Saigal, S., 2003. Co-planar crack interaction in cleaved mica. *Int. J. Fract.* 119 (4), 365–386.
- Hutchinson, J.W., 1987. Crack tip shielding by micro-cracking in brittle solids. *Acta Metall.* 35 (7), 1605–1619.
- Hutchinson, J.W., Suo, Z., 1991. Mixed mode cracking in layered materials. *Adv. Appl. Mech.* 29, 63–191.
- Kaelble, D., 1965. Peel Adhesion: micro-fracture mechanics of interfacial unbonding of polymers. *Trans. Soc. Rheol.* (1957–1977) 9 (2), 135–163.
- Lai, Y.-H., Dillard, D., Thornton, J., 1992. The effect of compressibility on the stress distributions in thin elastomeric blocks and annular bushings. *J. Appl. Mech.* 59 (4), 902–908.
- Larsen, H.-O., 1987. Mold for making contact lenses, either the male or female mold sections being relatively more flexible. U.S. Patent No. 4,640,489.
- Lefebvre, D.R., Dillard, D.A., Brinson, H., 1988. The development of a modified double-cantilever-beam specimen for measuring the fracture energy of rubber to metal bonds. *Exp. Mech.* 28 (1), 38–44.
- Li, S., Thouless, M., Waas, A., Schroeder, J., Zavattieri, P., 2005. Use of mode-I cohesive-zone models to describe the fracture of an adhesively-bonded polymer-matrix composite. *Compos. Sci. Technol.* 65 (2), 281–293.
- Li, S., Wang, J., Thouless, M., 2004. The effects of shear on delamination in layered materials. *J. Mech. Phys. Solids* 52 (1), 193–214.
- Maugis, D., 1992. Adhesion of spheres: the JKR-DMT transition using a Dugdale model. *J. Colloid Interface Sci.* 150 (1), 243–269.
- Messner, A., 1963. Stress Distributions in Poker Chip Tensile Specimens Aerojet-General Technical Paper.
- Mönch, W., Herminghaus, S., 2001. Elastic instability of rubber films between solid bodies. *EPL (Europhys. Lett.)* 53 (4), 525.
- Mukherjee, B., 2016. Interfacial debonding from a sandwiched elastomer layer. PhD, Virginia Polytechnic Institute and State University.
- Mukherjee, B., Dillard, D.A., Moore, R.B., Batra, R.C., 2016a. Debonding of Confined Elastomeric Layer using Cohesive Zone Model. *Int. J. Adhes. Adhes.* 66, 114–127.
- Mukherjee B, Batra RC, Dillard DA, 2016c. Edge debonding in peeling of a thin flexible plate from an elastomer layer: a cohesive zone model analysis. *ASME. J. Appl. Mech.* doi: 10.1115/1.4034988.
- Mukherjee, B., Dillard, D.A., Moore, R.B., Batra, R.C., 2016d. On preferential debonding during demolding of a sandwiched elastomeric layer. In preparation.
- Sarkar, J., Sharma, A., Shenoy, V., 2005. Adhesion and debonding of soft elastic films: Crack patterns, metastable pathways, and forces. *Langmuir* 21 (4), 1457–1469.
- Shen, B., Paulino, G., 2011. Direct extraction of cohesive fracture properties from digital image correlation: a hybrid inverse technique. *Exp. Mech.* 51 (2), 143–163.
- Shenoy, V., Sharma, A., 2001. Pattern formation in a thin solid film with interactions. *Phys. Rev. Lett.* 86 (1), 119.
- Sinko, R., Ketten, S., 2015. Traction-separation laws and stick-slip shear phenomenon of interfaces between cellulose nanocrystals. *J. Mech. Phys. Solids* 78, 526–539.
- Song, S.H., Paulino, G.H., Buttlar, W.G., 2006. A bilinear cohesive zone model tailored for fracture of asphalt concrete considering viscoelastic bulk material. *Eng. Fract. Mech.* 73 (18), 2829–2848.
- Suo, Z., Hutchinson, J.W., 1989. Sandwich test specimens for measuring interface crack toughness. *Mater. Sci. Eng.* 107, 135–143.
- Tang, T., Hui, C.Y., 2005. Decohesion of a rigid punch from an elastic layer: Transition from “flaw sensitive” to “flaw insensitive” regime. *J. Polym. Sci., Part B: Polym. Phys.* 43 (24), 3628–3637.
- Tizard, G., Dillard, D., Norris, A., Shephard, N., 2012. Development of a high precision method to characterize Poisson's ratios of encapsulant gels using a flat disk configuration. *Exp. Mech.* 52 (9), 1397–1405.
- Tsai, C., Guan, Y., Ohanehi, D., Dillard, J., Dillard, D., Batra, R., 2014. Analysis of cohesive failure in adhesively bonded joints with the SSPH meshless method. *Int. J. Adhes. Adhes.* 51, 67–80.
- Turon, A., Davila, C.G., Camanho, P.P., Costa, J., 2007. An engineering solution for mesh size effects in the simulation of delamination using cohesive zone models. *Eng. Fract. Mech.* 74 (10), 1665–1682.
- Ungsuwarungsri, T., Knauss, W.G., 1987. The role of damage-softened material behavior in the fracture of composites and adhesives. *Int. J. Fract.* 35 (3), 221–241.
- Vilmin, T., Ziebert, F., Raphaël, E., 2009. Simple View on Fingering Instability of Debonding Soft Elastic Adhesives. *Langmuir* 26 (5), 3257–3260.
- Webber, R.E., Shull, K.R., Roos, A., Creton, C., 2003. Effects of geometric confinement on the adhesive debonding of soft elastic solids. *Phys. Rev. E* 68 (2), 021805.
- Xiao, J., Batra, R., 2014. Delamination in sandwich panels due to local water slamming loads. *J. Fluids Struct.* 48, 122–155.
- Xu, X.-P., Needleman, A., 1995. Numerical simulations of dynamic crack growth along an interface. *Int. J. Fract.* 74 (4), 289–324.
- Yamaguchi, T., Koike, K., Doi, M., 2007. In situ observation of stereoscopic shapes of cavities in soft adhesives. *EPL (Europhys. Lett.)* 77 (6), 64002.
- Zhou, X., Zimmerman, J., Reedy, E., Moody, N., 2008. Molecular dynamics simulation based cohesive surface representation of mixed mode fracture. *Mech. Mater.* 40 (10), 832–845.